

12-2017

Development of Pre-Stressed Retrofit Strategies for Mitigating Fatigue Cracking in Steel Waterway Lock Gate Components

Christine Michelle Lozano
University of Arkansas, Fayetteville

Follow this and additional works at: <http://scholarworks.uark.edu/etd>

 Part of the [Civil Engineering Commons](#), [Construction Engineering and Management Commons](#), and the [Environmental Engineering Commons](#)

Recommended Citation

Lozano, Christine Michelle, "Development of Pre-Stressed Retrofit Strategies for Mitigating Fatigue Cracking in Steel Waterway Lock Gate Components" (2017). *Theses and Dissertations*. 2541.
<http://scholarworks.uark.edu/etd/2541>

This Thesis is brought to you for free and open access by ScholarWorks@UARK. It has been accepted for inclusion in Theses and Dissertations by an authorized administrator of ScholarWorks@UARK. For more information, please contact scholar@uark.edu, ccmiddle@uark.edu.

Development of Pre-Stressed Retrofit Strategies for Mitigating Fatigue Cracking in Steel
Waterway Lock Gate Components

A thesis submitted in partial fulfillment
of the requirements for the degree of
Master of Science in Civil Engineering

by

Christine Lozano
LeTourneau University
Bachelor of Science in Engineering, 2016

December 2017
University of Arkansas

This thesis is approved for recommendation to the Graduate Council.

Gary S. Prinz, Ph.D
Thesis Director

Guillermo Riveros, Ph.D
Committee Member

Micah Hale, Ph.D
Committee Member

Abstract

Lock gates are an important part of the transportation infrastructure within the United States (US), having many economic, safety, and environmental benefits over rail and highway transportation systems. Unfortunately, many existing lock gates throughout the US have reached or exceeded their initial design life and require frequent repairs to remain in service. Unscheduled repairs often increase as gates age, having a local economic impact on freight transport which can create economic ripples throughout the nation. Fatigue and corrosion are key causes of unscheduled service interruptions, degrading lock gate components over time. Additionally, because lock gates are submerged during operation, crack detection prior to component failure can be difficult, and repair costs can be high.

This thesis presents an analytical and experimental investigation into fatigue damage within common lock gate geometries, and develops fatigue mitigation strategies capable of extending gate service-life. The goal of the research program is to identify critical fatigue regions and locally extend gate component fatigue life. Detailed finite element analyses are combined with fatigue and fracture mechanics theories to predict critical fatigue regions within common gate details and develop retrofit strategies for mitigating fatigue cracking. Full-scale experimental fatigue testing of a critical lock gate component is conducted to provide a baseline for evaluation of retrofit strategies. Retrofit strategies using carbon fiber reinforced polymer (CFRP) plates having optimized pre-stress levels are discussed.

Acknowledgements

This report presents the results of a research project sponsored by Maritime Transportation Research & Education Center (MarTREC). We acknowledge the financial and material support provided by MarTREC as well as the assistance and encouragement of Dr. Guillermo Riveros from the US Army Corps of Engineers. The research was conducted in the Steel Structures Research Laboratory (SSRL) at the University of Arkansas. Laboratory staff and graduate students instrumental in the completion of this work include: Maggie Langston, David Peachee, Diego Real and Mark Kuss.

This material is based on work supported by the U.S. Department of Transportation under Grant Award Number DTRT13-G-UTC50. The work was conducted through MarTREC at the University of Arkansas.

Table of Contents

1. Introduction.....	1
1.1. Overview.....	1
2. Review of relevant literature.....	7
2.1. Fatigue in steel lock gates and review of analysis methods.....	7
2.2. Review of fatigue retrofit methods	8
2.2.1. <i>Weld surface treatment</i>	8
1.1.1. <i>Hole-drilling in steel sections</i>	8
2.2.2. <i>Vee-and-weld</i>	9
2.2.3. <i>Doubler/splice plates</i>	9
2.2.4. <i>Post-tensioning</i>	9
2.3. Overview of cfrp and review applications in structural retrofits	10
3. Analytical investigation into lock gate component fatigue.....	13
3.1. Selection of lock gate for analysis	13
3.2. Modeling techniques.....	13
3.2.1. <i>Geometry and boundary conditions</i>	13
3.2.2. <i>Loading</i>	17
3.3. Determination of fatigue damage.....	18
3.3.1. <i>Miner's total damage</i>	18
3.3.2. <i>Cycle counting</i>	19
4. Results and discussion from gate analyses.....	20
4.1. Fatigue life evaluation.....	20
5. Description of detailed fatigue investigation for critical component	22
5.1. Fatigue endurance from constant life diagrams: the goodman criterion.....	23
6. Required pre-stressing force from goodman constant life diagram	26
6.1. Transfer of pre-stress through friction clamping	28
7. Effect of pre-stress on component fatigue susceptibility	30
7.1. Revised calculations following retrofit simulations	31
7.2. Pre-stress simulation results.....	32
8. Fatigue retrofit prototype for later experimental testing.....	34
9. Preliminary experimental verification.....	36
9.1. Test matrix and experimental setup	36
9.2. Loading	38
9.3. Test specimen no. 1.....	38
9.3.1. <i>Model of test specimen</i>	39

9.4. Instrumentation and monitoring.....	40
9.5. Preliminary test results.....	41
9.5.1. Observations	41
9.5.2. Strain gage measurements	42
9.5.3. Dye penetrant.....	43
10. Summary and conclusions.....	44
11. References.....	46
APPENDIX A. Identification of critical sections	50
APPENDIX B. Reservoir cycle counting procedure.....	54
APPENDIX C. Goodman s_e calculations	56
APPENDIX D. Friction test derivation.....	61
APPENDIX E. Friction clamp calculations.....	62
APPENDIX F. Cycle estimation for experimental test.....	63

List of Figures

Figure 1. Function of lock gates within the lock system. 1) the lower gate is lowered allowing entrance to the lock. 2) the lower gate closes and the water level changes. 3) the upper gate opens allowing the vessel access to the higher water elevation.....	1
Figure 2. Marine highway routes within the us (marad, 2017).....	2
Figure 3. Transportation costs per ton (port of pittsburg, 2014).....	2
Figure 4. Cargo capacity equivalency (us army corps, 2017).....	2
Figure 5. Elevation view of greenup lock and dam geometry	5
Figure 6. Example of an un-bonded cfrp retrofit (prinz, 2016)	6
Figure 7. Project task timeline	6
Figure 8. Stress flow and concentration around a hole (adapted from figure in (anderson, 2005))	7
Figure 9. Vee and weld fatigue repair method.....	9
Figure 10. Stress amplitude reduction (doubler/splice plates) and shifted mean stress (post-tensioning).....	10
Figure 11. Section view diagram of cfrp	11
Figure 12. Bonded cfrp strips used to strengthen concrete structure (alkhrdaji, 2015).....	12
Figure 13. Cfrp vs steel elastic modulus.....	12
Figure 14. Upstream elevation and top view of a lock gate (greenup lock and dam, ohio river)	14
Figure 15. Section through leaf and recess of lock gate #1 (greenup lock and dam, ohio river)	14
Figure 16. Lock gate #1: detail of diagonal connection.....	15
Figure 17. Lock gate #1: section view of the quoin end.....	16
Figure 18. Lock gate #1: section view of miter end	16
Figure 19. Lock gate #1: upstream elevation diagram and applied boundary conditions for one lock gate leaf	16
Figure 20. Lock gate in empty lock	17
Figure 21. Different hydrostatic load levels applied on the gate (ft. – in.) And simulation of water level elevation change through hydrostatic load amplitude triggering	17

Figure 22. Greenup lock and dam von misses stress contour and numbered sections of high stress concentrations with stress graphs	18
Figure 23. Von misses stress concentrations at the point of highest loading and the connection detail for the section	20
Figure 24. A) a submodel embedded in gate model with mesh view; b) 3-d of submodel with contours from loading applied to gate.....	22
Figure 25. Triangular (fillet) weld geometry modeled as part of the solid element model	23
Figure 26. Components of cyclic stress	25
Figure 27. A) unmodified goodman diagram and yield line; b) modified goodman life diagram.	25
Figure 28. Modified goodman life diagram with data point and stress shift	27
Figure 29. Free body diagram of the pre-stress force	28
Figure 30. Free body diagram of clamp, retrofit, and section 13 to determine the required friction force from known pre-stress force.....	28
Figure 31. Corroded (bottom) and uncorroded (top) steel surfaces.....	29
Figure 32. Static coefficient of friction test: a) static coefficient of friction free body diagram; b) test materials	29
Figure 33. Retrofit application on section f13 in the fea model	30
Figure 34. New pre-stress force cross-section	31
Figure 35. Free body diagram used to calculate the pre-stress force.....	31
Figure 36. Stress range shift, in section f13, due to applied cfrp pre-stress (1 lockage cycle) 32	
Figure 37. Goodman life diagram with stress shift change of section f13 with the retrofit applying 35.2 kips pre-stress force.....	33
Figure 38. Retrofit components and assembled cfrp retrofit	35
Figure 39. Cross-section of pre-stress bearing mechanism with forces applied by bolts to create the pre-stress.....	35
Figure 40. Cross-section view of retrofit friction grip mechanism.....	35
Figure 41. Diagram of top view test setup and test matrix	37
Figure 42. Diagram of test-setup side view	37
Figure 43. Test setup.....	37
Figure 44. 3-d of the specimen with attachment plates, load, and boundary condition.....	38

Figure 45. Section 13 specimen fabrication details	39
Figure 46. Boundary conditions for abaqus simulation of test setup.....	40
Figure 47. A) stresses from submodel of lock gate; b) stresses from model of test specimen	40
Figure 48. A) strain gage location; b) specimen with attached strain gages.....	41
Figure 49. Dye penetrant application steps (ovouba, 2017)	41
Figure 50. Notch at weld corner (8 million cycles)	42
Figure 51. Recorded strains, a) pre-notch; b) post-notch.....	42
Figure 52. Dye penetrant progression: a) 6 million cycles; b) 10 million cycles	43

List of Tables

Table 1. List of gates on the arkansas river system, completed date, and date of repair	3
Table 2. Types of cfrp based on modulus of elasticity and strength (kopeliovich, 2012)	11
Table 3. Fatigue damage calculations of critical sections.....	21
Table 4. Aashto life-cycle fatigue from model data	33
Table 5. Stresses from gate model of greenup lock & dam gate 1 (35.2 kip pre-stress)	33

Notation

The following terms are used in the text of this report:

γ	=	fatigue load factor;
Δf	=	live load stress range due to the passage of the fatigue load;
ΔF_n	=	nominal fatigue resistance;
ΔF_{TH}	=	constant amplitude fatigue threshold;
A	=	detail category AASHTO Table 6.6.1.2.3-1 (ksi^3);
N	=	number of expected cycles to reach the nominal fatigue resistance;
D_i	=	total damage;
n_i	=	number of cycles;
N_i	=	number of cycles to failure;
$\Delta\sigma$	=	applied stress range;
S_e	=	fatigue endurance limit;
S'_e	=	estimated fatigue endurance limit;
k	=	modification factors in the Marin Equation;
Ω	=	unit of electrical resistance;

Disclaimer

The contents of this report reflect the views of the authors, who are responsible for the facts and the accuracy of the information presented herein. This document is disseminated under the sponsorship of the U.S. Department of Transportation's University Transportation Centers Program, in the interest of information exchange. The U.S. Government assumes no liability for the contents or use thereof.

1. Introduction

1.1. Overview

Locks are essential for waterway transport along many river and canal systems, allowing passage of ships through regions of differing water elevation. Locks operate by creating a chamber of water that can be lowered or raised independently from the upstream or downstream elevations. Figure 1 shows a typical miter lock gate and the water elevation change process. As shown in Figure 1, two sets of gates open and close in sequence as the ship transitions to a higher water elevation.

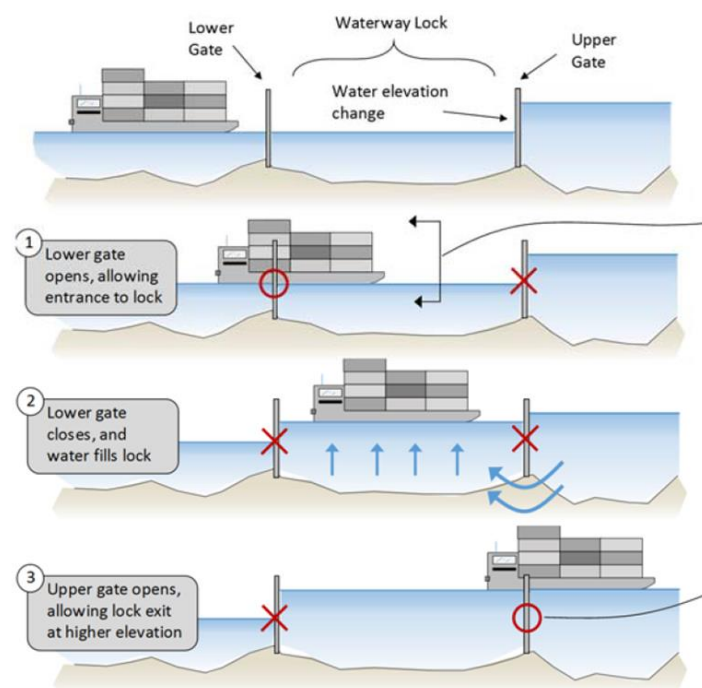


Figure 1. Function of lock gates within the lock system. 1) The lower gate is lowered allowing entrance to the lock. 2) The lower gate closes and the water level changes. 3) The upper gate opens allowing the vessel access to the higher water elevation.

The United States waterway transportation infrastructure (including lock gates) is extensive, including over 12,000 miles of waterway (see Figure 2), and has economic, security, and environmental benefits over traditional rail or highway transport systems (U.S. Army Corps of Engineers, 1999). Other forms of transport such as rail or truck can be 5-10 times more expensive than waterway transport respectively (see Figure 3) (The Port of Pittsburgh Commission, 2017). As an example, barge transport along inland waterways of the upper

Mississippi River generates a transportation cost savings of nearly \$1 billion dollars annually (U.S. Army Corps of Engineers Mississippi Valley Division, 2016). The most common type of barge used to transport goods along the major waterways is a 15-barge tow, which is equivalent to nearly 5 unit trains and 870 trucks (see Figure 4)

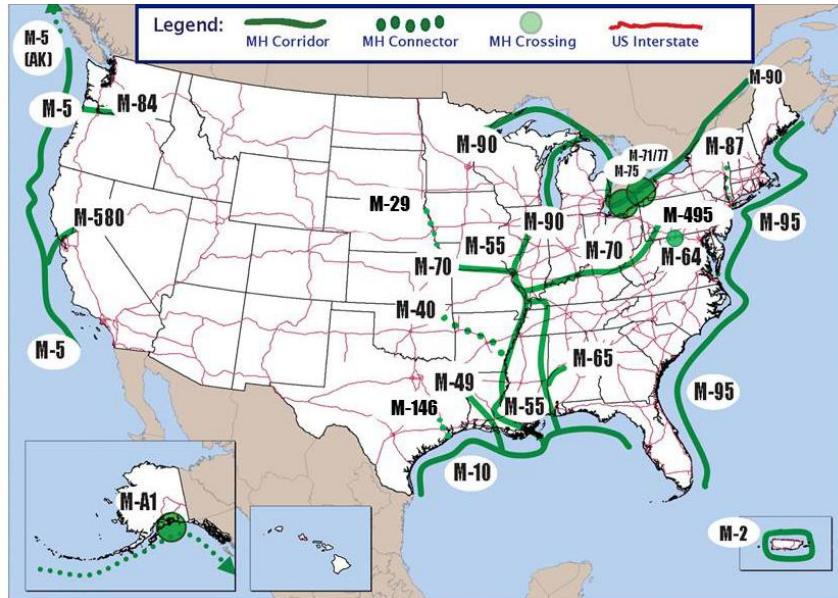


Figure 2. Marine highway routes within the US (MARAD, 2017)



Figure 3. Transportation costs per ton (Port of Pittsburg, 2014)

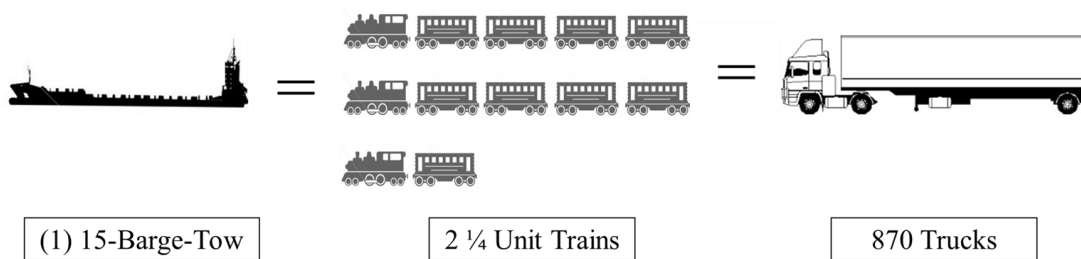


Figure 4. Cargo capacity equivalency (US Army Corps, 2017)

While locks are essential to waterway transport, many of the lock gates within the United States have reached or exceeded their design life. Many of the existing lock gates were designed for a service life of 50 years (U.S. Army Corps of Engineers, 2017) but have aged beyond this service-life expectancy, with additional locks getting older each year. Some locks have even doubled their expected service life, having been constructed in the early 1900's. The Hiram M. Chittenden Locks in Seattle, Washington, will turn 100 years old in 2017. As lock gates reach their design life, costly repairs are often needed to maintain waterway access. Table 1 shows, the scheduled repairs for the locks on the Arkansas River System, with required repairs occurring after forty years of service (on average) (U.S. Army Corps of Engineers, 2017).

Table 1. List of gates on the Arkansas River System, completed date, and date of repair

Lock/Dam	Started/Completed	Repairs	Years Before Repairs (yrs.)
Arthur V. Ormond Lock and Dam No. 9	1965/1969	N/A	N/A
Choteau Lock No. 17	1967/1970	2012	42
Dardanelle Lock and Dam No. 10	1957/1969	2017	48
David D. Terry Lock and Dam No. 6	1965/1968	2009	41
Emmett Sanders Lock and Dam No. 4	1964/1968	N/A	N/A
J. W. Trimble Lock and Dam No. 13	1965/1969	N/A	N/A
Joe Hardin Lock and Dam No. 3	1963/1968	2013	45
Lock and Dam No. 5	1964/1968	N/A	N/A
Montgomery Point Lock and Dam	1998/2004	2015	11
Murray Lock and Dam No. 7	1964/1969	2015	46
Newt Graham Lock No. 18	1967/1970	N/A	N/A
Norrell Lock and Dam No. 1	1963/1967	N/A	N/A
Norrell Lock No. 2	1963/1968	2013	45
Ozark-Jeta Taylor Lock and Dam No. 12	1964/1969	N/A	N/A
Robert S. Kerr Lock and Dam No. 15	1964/1970	N/A	N/A
Toad Suck Ferry Lock and Dam No. 8	1965/1969	Canceled	Canceled
W. D. Mayo Lock No. 14	1966/1970	2014	44
Webber Falls Lock and Dam No. 16	1965/1970	2016	46
Average age before repair			40

Unscheduled repairs often increase as gates age, having a local economic impact on freight transport and creating economic ripples throughout the national infrastructure. Regarding the economic impact of service interruptions, *temporary* structural repairs to the Montgomery Lock & Dam on the Ohio River totaled over \$3.5 million, and were intended as

a short term solution only to last 5 years (Hawk 2011). Note that this \$3.5 million cost does not include the economic losses associated with transport rerouting. Lock gate fatigue failures in the Algiers Lock along the Mississippi River resulted in \$5.2 million of required repairs, and interrupted waterway transport (McKee 2013). Aging of existing locks and service interruptions can ripple through other aspects of our nation's infrastructure. For example, aging locks along the Mongongahela River Navigation System facilitate transport of approximately 20M tons of cargo annually (most of which is coal to generate electric power), with the potential for a significant economic and power-grid impact given a gate failure or unscheduled maintenance closure (Hawk 2011). An unscheduled extension of repairs on the Greenup Lock and Dam (which occurred during winter months) caused energy plants to ship coal by alternate means as stockpiles became depleted (Glass, 2012). During these extended repairs on the Greenup Lock and Dam the MEMCO Barge Line company lost \$1.3 million (Glass, 2012).

Fatigue and corrosion are key causes of lock gate component failures leading to unscheduled service interruptions. Fatigue damage occurs as structural components are subjected to frequently repeated loads, which in the case of a lock gate may include frequent water elevation changes or gate openings. Figure 5 shows a typical miter gate section and water elevation changes that occur during normal operation. Specific parameters leading to fatigue damage include the applied component stress range (σ_a), applied mean stress (σ_m), as well as the aggressiveness of the structural environment. Typically, increases in stress range, mean stress, or the aggressiveness of the environment will lead to increased fatigue damage. Submerged water environments where lock gates are required to operate, promotes corrosion and unlike many other steel structures subjected to repeated loading, corrosion promoted fatigue does not have a fatigue limit, so failures are difficult to predict (NACE International, 2017). Fatigue tends to occur first in connection details, especially those containing welds, due to locked-in residual stresses or geometry induced stress concentrations which shift locally the

applied mean stress. Lock gates are primarily constructed of welded steel sections and many gates are at high risk for fatigue failures following years of service in a corrosive environment (U.S. Army Corps of Engineers, 2017).

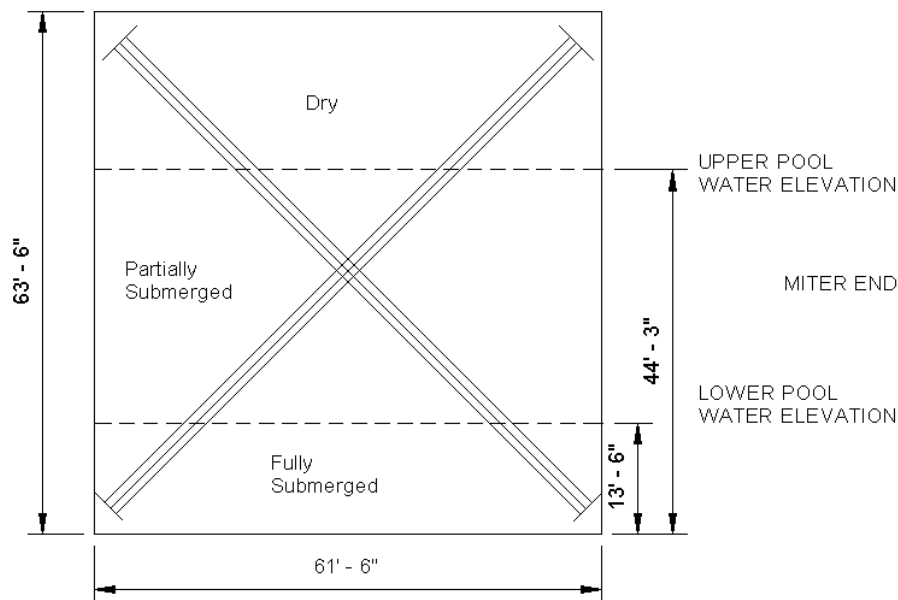


Figure 5. Elevation view of Greenup Lock and Dam geometry

Additionally, lock gates are partially submerged in water which can make it difficult to detect existing cracks. Because of this, existing cracks are often allowed to grow until failure disrupts normal gate service. Once a gate has experienced cracking and needs repair, the lock must be de-watered to allow access and favorable repair conditions.

The difficulty of crack detection and high repair costs have led to research on lock gate fatigue cracking and failures. Carbon fiber reinforced polymer (CFRP) materials have been used successfully as a crack mitigation method as they have a high strength to weight ratio, high resistance to environmental corrosion, and a high ease of onsite implementation (Prem Pal Bansal, 2016) (Alaa AL-Mosawe, 2015). Additional CFRP research involving post-tensioned retrofits seems promising. Post-tensioned CFRP has been used in two different applications: 1) bonded to existing cracks, like a patch (Prem Pal Bansal, 2016) (Alaa AL-

Mosawe, 2015), and 2) in an un-bonded configuration (E. Ghafouri M. M., 2016) (Fabio Matta, 2007) (Sunnam Hong, 2015) as seen in Figure 6.

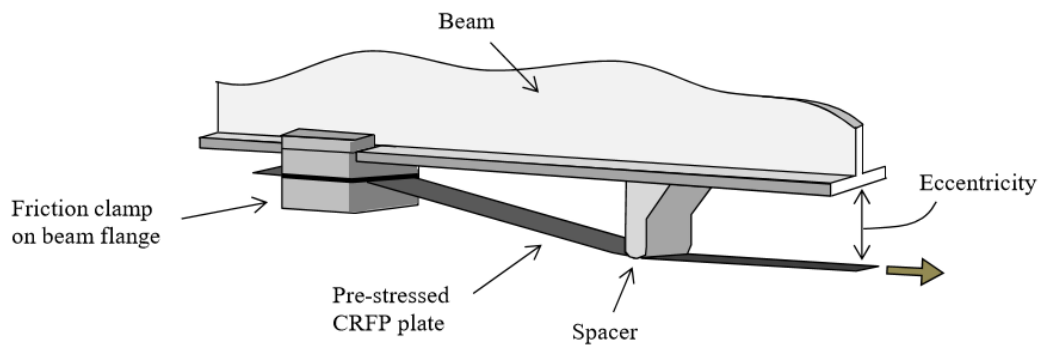


Figure 6. Example of an un-bonded CFRP retrofit (Prinz, 2016)

This thesis presents an analytical and experimental investigation into fatigue damage within common lock gate geometries, and develops fatigue mitigation strategies capable of extending gate service-life. The goal of the research program is to identify the critical fatigue region and locally extend the lock-gate component fatigue life. Common lock gate geometries are identified with help from the US Army Corps of Engineers (project contact: Dr. Guillermo Riveros) and are analyzed using detailed finite element analyses. Stress data gathered from the analyses are used to inform novel pre-stressed fatigue retrofit strategies, and identify any retrofit geometry constraints. Corrosion-resistant CFRP material with potential application for the fatigue retrofits is investigated. Figure 7 shows the research project tasks, with Tasks 1 and 2 being presented in this report. Note that future research will involve field instrumentation of actual lock gate components which will inform on the long term performance of the developed fatigue retrofits under actual gate service conditions.

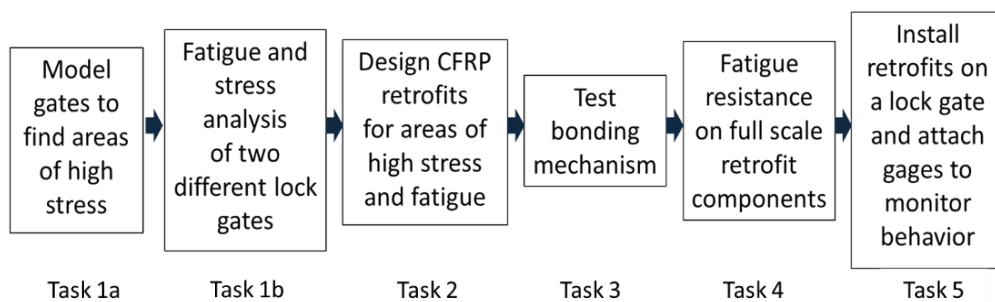


Figure 7. Project task timeline

2. Review of Relevant Literature

2.1. Fatigue in Steel Lock Gates and Review of Analysis Methods

Lock gates are prone to fatigue cracking due to the severity of the applied cyclic loads and aggressiveness of the corrosive environment. Connection regions where members are welded, bolted, and contain irregular geometric features often create stress concentrations that lead to high stress fluctuations and fatigue damage. Figure 8 shows how stress concentrations can develop around geometric features, as the stresses “flow” around geometric features (Anderson, 2005). Welded sections also tend to be more susceptible to fatigue cracking as they introduce heat-induced flaws in the metal microstructure. (Mertz, 2012).

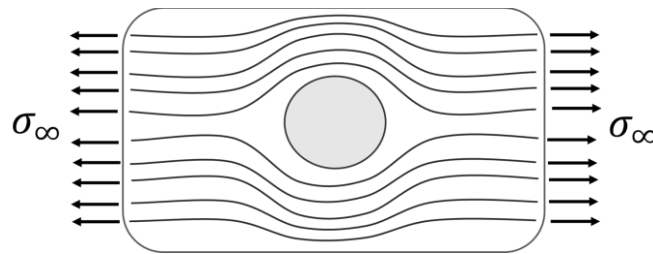


Figure 8. Stress flow and concentration around a hole (adapted from figure in (Anderson, 2005))

While it can be difficult to account for local geometric features and their effects on local stress ranges, the American Association of State Highway Transportation Officials (AASHTO) has developed common component details and their corresponding fatigue capacities based on applied nominal stresses (American Association of State Highway and Transportation Officials, 2012). The detail categories (A, B, B', C, C', D, E, and E') found in (American Association of State Highway and Transportation Officials, 2012) are determined based largely on experimental testing of different component geometries. All fatigue detail capacities take the form of Equation 1:

$$(\Delta F)_n = (A/N)^{\frac{1}{3}} \quad \text{Equation 1}$$

where A is a constant representing the intercept of the stress versus number of cycles to failure (S-N) curve taken from AASHTO Table 6.6.1.2.5-1 based on the detail type; N is the number

of expected cycles to reach the nominal fatigue resistance ($(\Delta F)_n$) (American Association of State Highway and Transportation Officials, 1988).

2.2. Review of Fatigue Retrofit Methods

There are many different fatigue retrofit methods currently in use; however, all methods aim to do one of two things: 1) reduce the applied component stress range (often by stiffening or softening the section), or 2) reduce the applied component mean stress (often through an induced pre-stress). Common methods include weld surface treatments, hole-drilling, vee-and-weld, adding doubler/splice plates, and post-tensioning. The following sections give a review of each of these methods.

2.2.1. Weld Surface Treatment

Surface treatments improve un-cracked weld strength by reducing abrupt geometric changes or removing locked-in tensile residual stresses. Surface treatments include grinding, gas tungsten arc or plasma re-melting of the weld toe, and impact treatments. Surface treatments improve fatigue strength by improving the weld geometry and reducing stress concentrations, eliminating discontinuities where fatigue cracks may propagate, and reducing residual tensile stresses. After the surface treatment has been applied, the damaging effects of any prior loading cycles are removed, and the next greatest S-N curve can be used to predict the life of the section. Surface treatments only affect the weld toes (Robert J. Dexter, 2013).

1.1.1. Hole-Drilling in Steel Sections

Hole drilling is a common method for alleviating high stress concentrations at the tip of existing fatigue cracks. This method incorporates fatigue analysis fundamentals, by removing the sharp notch at the crack tip, stopping the propagation of the crack under Mode I loadings but less effective for mixed mode loading. The hole also lessens the stress concentration by shifting the stresses around the sides of the hole, see again Figure 8. The hole size must be large enough to contain the full crack tip with required hole sizes sometimes

ranging between 2-4 inches (Robert J. Dexter, 2013). The hole drilling method is a simple way of slowing down crack growth by re-directing the stress path.

2.2.2. Vee-and-Weld

The vee-and-weld method is often used in conjunction with other methods to reduce the actual stress range experienced by the original crack (Robert J. Dexter, 2013). Once a crack has been found, the area around the crack length is removed in a “V” shape and then refilled with weld metal, see Figure 9. One drawback of this method is that the weld must be done by a certified welder, and significant care must be taken to produce a quality weld. Additionally, studies conducted on the vee-and-weld method concluded that the resulting repaired fatigue life is only as good as the original detail (Robert J. Dexter, 2013) (Stefano Caramelli, 1997) (Kentarō Yamada, 1986)

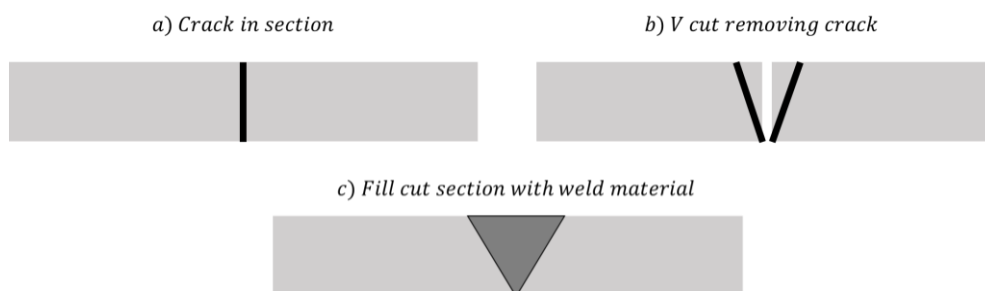


Figure 9. Vee and weld fatigue repair method

2.2.3. Doubler/Splice Plates

The addition of doubler or splice plates near fatigue prone details aim to reduce the applied stress range within the original component (Robert J. Dexter, 2013) . As the section area increases, the applied stress range is reduced (see Figure 10) and fatigue life is extended. One of the drawbacks of the doubler/splice plate method is the significant addition of weight to the structure.

2.2.4. Post-Tensioning

Fatigue cracks form by repeated stresses in tension causing a section to open and close. Post-tensioning considers the tensile stresses needed to create and propagate cracks by shifting

the effective mean stress into a region of slight compression. Pre-stressed retrofits are placed on the section and introduce the tension required to shift the mean stress, see Figure 10. There are different methods to apply post-tension: pre-stressing strands, post-tensioning bars, or nuts torqued on high-strength rods. All the previously stated methods add tension to shift the effective mean stress partly or completely into compression (Robert J. Dexter, 2013).

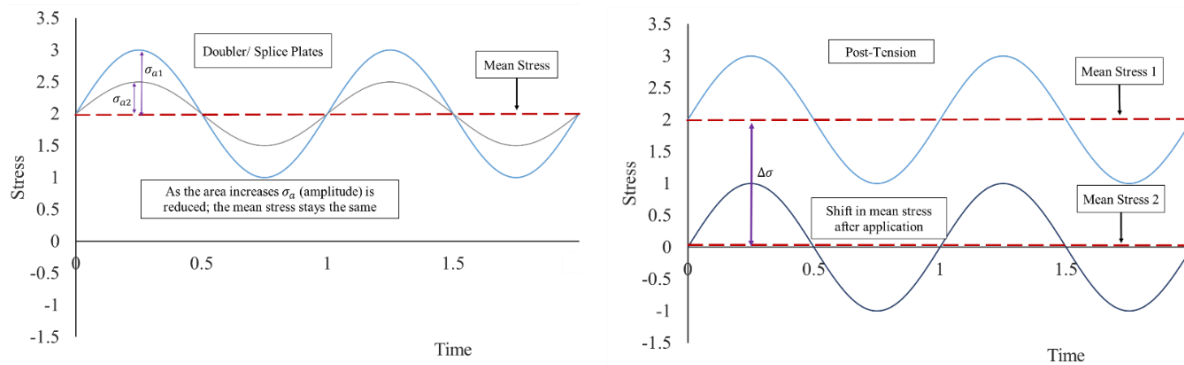


Figure 10. Stress amplitude reduction (Doubler/Splice Plates) and Shifted Mean Stress (Post-Tensioning)

2.3. Overview of CFRP and Review Applications in Structural Retrofits

CFRP is a composite material made of carbon fiber strands within a resin matrix, see Figure 11. As seen in Figure 11, the carbon fiber strands are laid laterally and longitudinally. The weave pattern allows CFRP to be flexible and moldable while still having significant strength in tension. Additionally, CFRP is corrosion resistant and has a high fatigue life. There are different types of CFRP with varying properties allowing for a broader use of the material. Table 2 gives a list of five of the most readily available types of CFRP. CFRP is currently used within different fields including the automotive, aerospace, sporting goods, and infrastructure because of its strength, flexibility, corrosion resistance, high strength to weight ratio, and moldability.

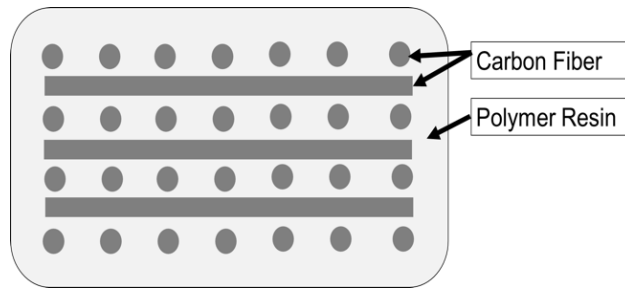


Figure 11. Section view diagram of CFRP

Table 2. Types of CFRP based on modulus of elasticity and strength (Kopeliovich, 2012)

Type	Main Property
Ultra-High Modulus (UHM)	Modulus of Elasticity: >65,400 ksi
High Modulus (HM)	Modulus of Elasticity: 51,000-65,400 ksi
Intermediate Modulus (IM)	Modulus of Elasticity: 29,000-51,000 ksi
High Tensile, Low Modulus (HT)	Tensile Strength: >436 ksi
	Modulus of Elasticity: <14,500 ksi
Super High Tensile (SHT)	Tensile Strength: >650 ksi

Recently CFRP has been introduced as a strength and crack reduction retrofit in concrete and steel sections. CFRP has been used in concrete as a wrap-like retrofit to improve the tensile capacity of the section, see Figure 12. Current research has been conducted to determine the capacity of CFRP compared to steel and see how it works as a fatigue or strengthening retrofit (E. Ghafoori M. M., 2016) (Fabio Matta, 2007) (M. Tavakkolizadeh, 2003). The elastic modulus of CFRP is similar to that of steel, but CFRP has a higher ultimate strength, see Figure 13. CFRP is less prone to corrosion than steel and has a lower weight to strength ratio (CFRP is about 20% of the mass of steel but with the same strength and elastic modulus (Alkhrdaji, 2015)). Several studies have shown the advantages of using CFRP to increase flexural performance, by reinforcing tensile components, and extending fatigue life, by reducing the stress range or shifting the mean stress down (A. Peiris, 2015) (D. Schnerch, 2008) (T.C. Miller, 2001) (B. Kaan, 2012) (Y. Huawen, 2010) (E. Ghafoori M. M., 2015) (Hussam Mahmoud, 2017).



Figure 12. Bonded CFRP strips used to strengthen concrete structure (Alkhrdaji, 2015)

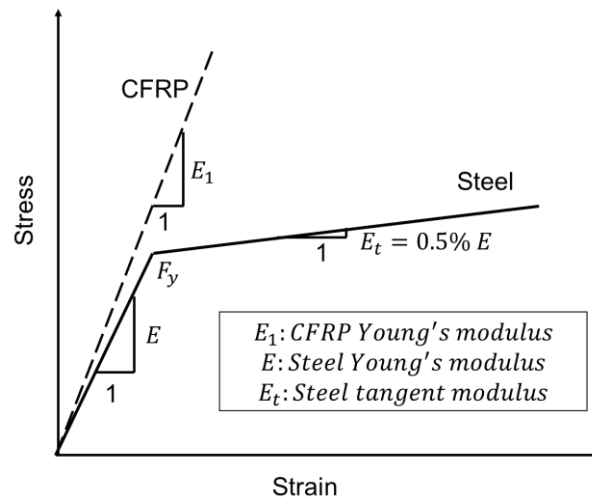


Figure 13. CFRP vs Steel elastic modulus

Pre-stressed CFRP has successfully been used, by Ghafoori et al (2016), to shift the mean stress in railroad bridges below the fatigue endurance limit increasing fatigue life. Research has proven that pre-stressed CFRP has increased the fatigue life of a steel section by up to 20 times (E. Ghafoori M. M., 2011) (Y. Huawen, 2010) with the thickness and pre-stress level of the CFRP being two important factors that influence how the retrofit performs. The current research aims to develop CFRP retrofits to reinforce critical fatigue details on lock gates.

3. Analytical Investigation into Lock Gate Component Fatigue

3.1. Selection of Lock Gate for Analysis

The selection of lock gates for analysis in this thesis were conducted with the assistance of the Army Corps of Engineers; the Corps oversees 239 lock systems throughout the United States. All lock gates considered are in-service, and in difficult environments to study without dewatering. The gate selection for this research project was based on maintenance and dewatering schedules of existing gates in conjunction with the project timeline. One gate selected for this project was the Greenup Lock and Dam on the Ohio River.

3.2. Modeling Techniques

3.2.1. Geometry and Boundary Conditions

A detailed finite element model considering local geometric features was created from construction documents obtained for the Greenup Lock and Dam on the Ohio River. All boundary conditions considered represent the operation of the constructed gate. The gate was modeled using the commercial finite element software ABAQUS (Abaqus, 2017). Only one side of the lock gate was modeled due to symmetry. The dimensions of the gate are 63.5 feet by 61.5 feet by 5.71 feet, see Figure 14 and Figure 15. The gate was constructed from Grade 50 steel sections welded together. The gate diagonals (constructed from pre-tensioned rods) were simulated using linear spring elements pre-stressed to 22.9 ksi following the gate construction documents.

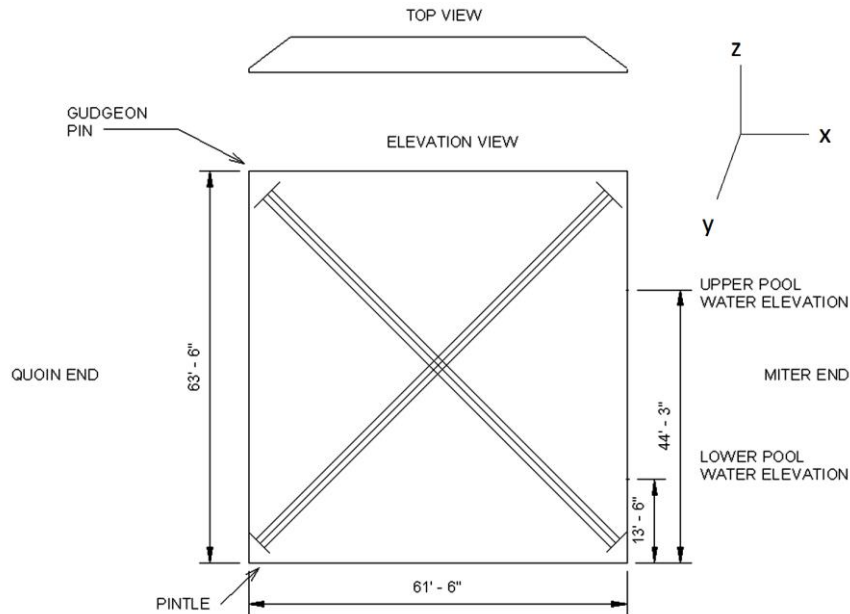


Figure 14. Upstream elevation and top view of a lock gate (Greenup Lock and Dam, Ohio River)

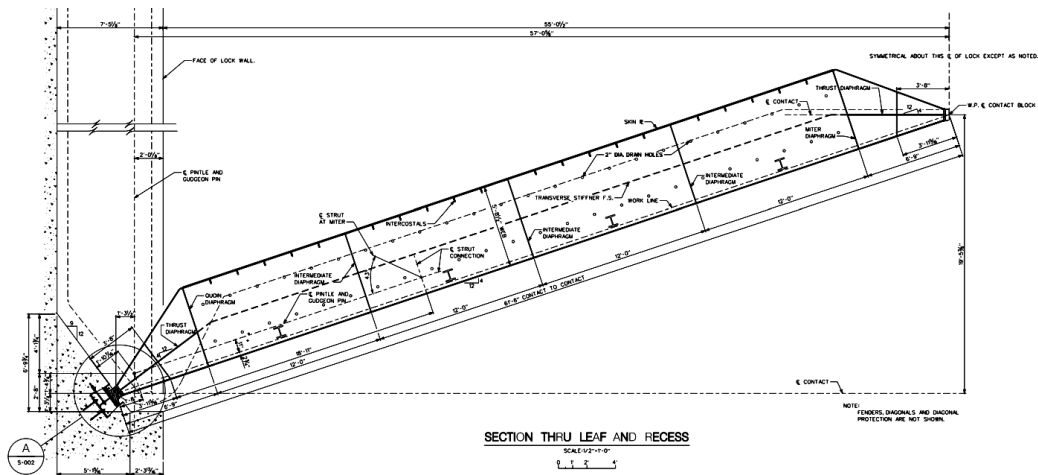


Figure 15. Section through leaf and recess of Lock Gate #1 (Greenup Lock and Dam, Ohio River)

Shell elements were used to simulate the gate geometric features. A general mesh size of 2.5 inches was used throughout, balancing computation expense and stress accuracy near geometric features having high stress gradients. In locations where the diagonal spring elements connect to the gate structure, nodes were tied to create rigid body regions simulating the details seen in Figure 16, and avoid local stress concentrations at the spring gate attachment. At the gudgeon pin and pintle (see again Figure 14) nodes were tied to create rigid bodies to

simulate the quoin blocks that are the point of rotation (shown in construction details of Figure 17 and Figure 18).

Boundary conditions chosen followed previous analyses performed by (Riveros, 2009). The boundary conditions were added to the following sections: the gudgeon pin was restrained in the X and Y directions as shown in Figure 19; the quoin and lock ends were restrained in the Y and Z directions; and the pintle was restrained in the X, Y, Z, XR, and YR, see Figure 19. The boundary conditions on the quoin and miter ends were applied along the full length of the gate. The quoin and miter end boundary conditions restrict movement in the X and Y directions simulating the concrete dam on the quoin end and the other lock gate leaf on the miter end, see Figure 19 and Figure 20.

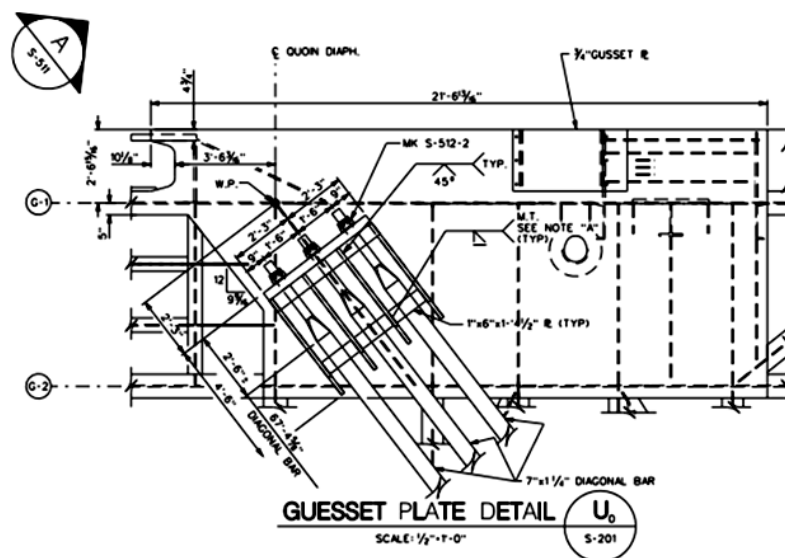


Figure 16. Lock Gate #1: detail of diagonal connection

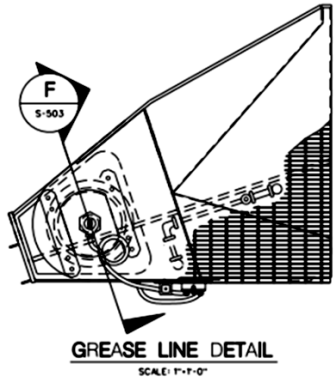


Figure 17. Lock Gate #1: section view of the quoin end

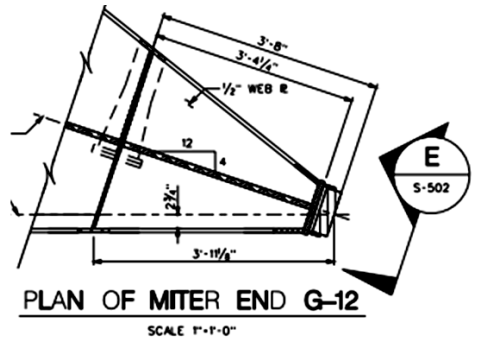


Figure 18. Lock Gate #1: section view of miter end

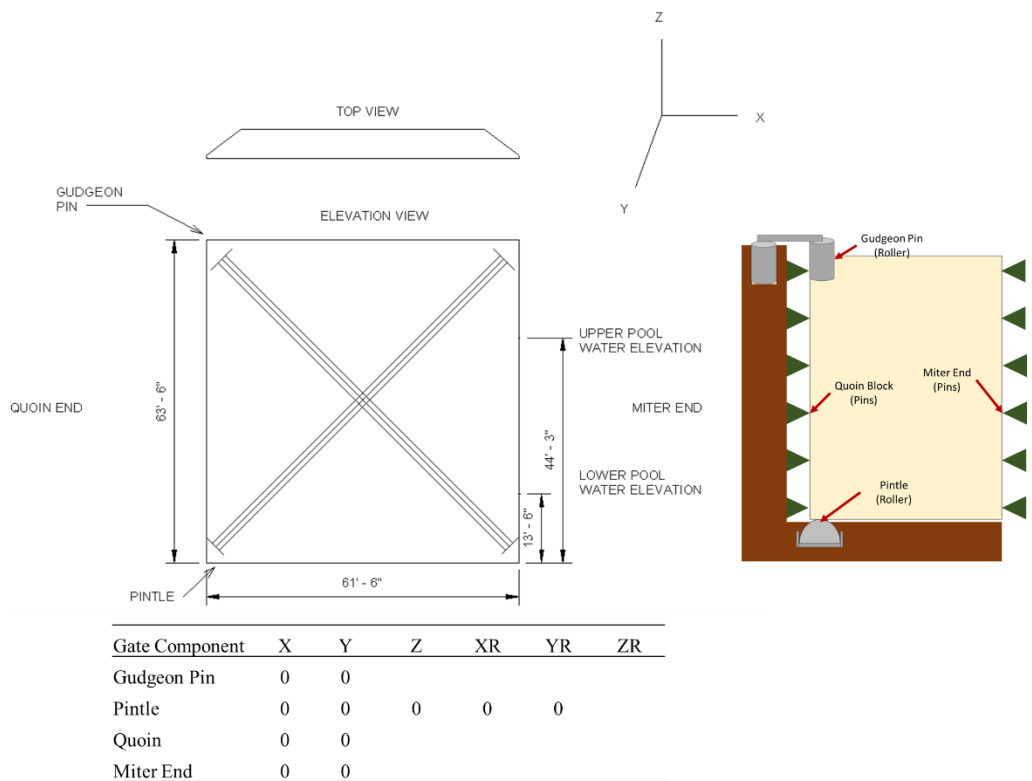


Figure 19. Lock Gate #1: upstream elevation diagram and applied boundary conditions for one Lock Gate leaf

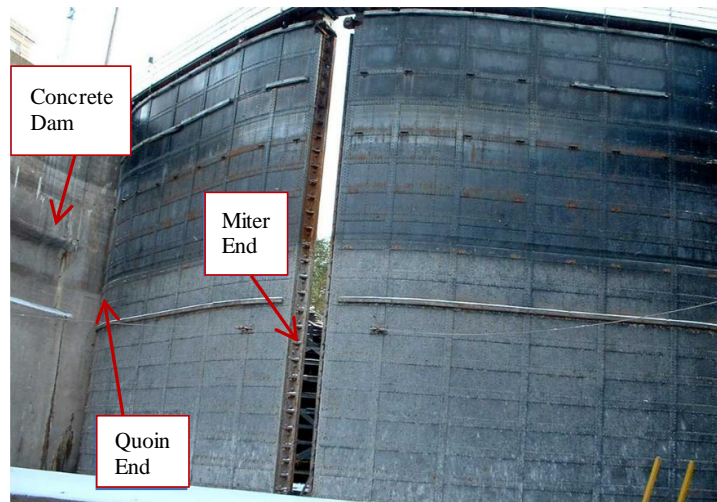


Figure 20. Lock gate in empty lock

3.2.2. Loading

All gate analyses consider gravity and hydrostatic loading. Changing water levels during lock operation are modeled using hydrostatic loads applied in sequential amplitudes to simulate a continuous rising water elevation. The load on the downstream face was set at the highest water level and remained constant during the analyses (see Figure 21). In Figure 21 the varying hydrostatic pressures applied to the upstream face are illustrated as a sequence of applied triangular ramping loads which provide a constantly increasing hydrostatic pressure corresponding to the increasing water level. The various load amplitudes turn one load on and off at different analysis “steps”; however, the magnitude of any two amplitudes always adds to one, allowing smooth transition from elevation to elevation.

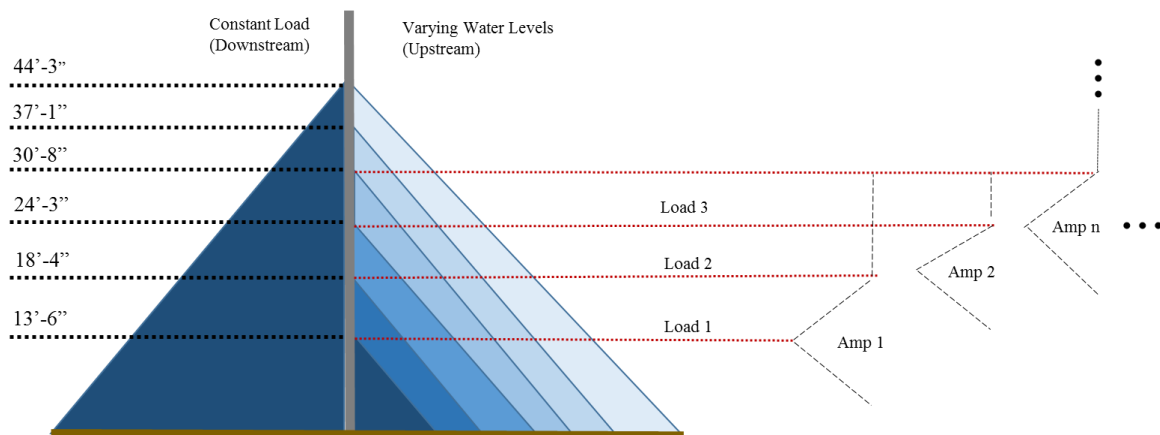


Figure 21. Different hydrostatic load levels applied on the gate (ft. – in.) and simulation of water level elevation change through hydrostatic load amplitude triggering

3.3. Determination of Fatigue Damage

The purpose of the gate model is to determine regions of high fatigue susceptibility. This is achieved by first identifying regions of high local stress fluctuation. As seen in Figure 22, high-stress regions can be determined from stress contours. The regions of high stress are compared to the AASHTO fatigue categories considering nominal applied stress ranges. Twenty-seven sections were determined to have high-stress concentrations. These sections are presented in Appendix A.

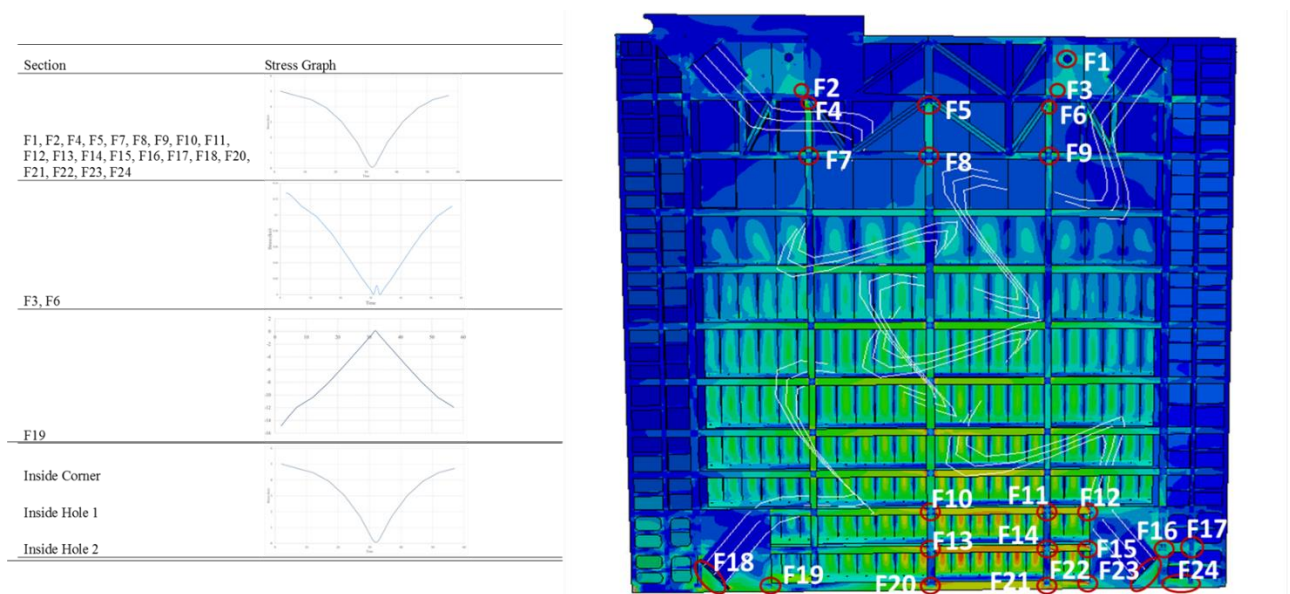


Figure 22. Greenup Lock and Dam von Misses Stress contour and numbered sections of high stress concentrations with stress graphs

3.3.1. Miner's Total Damage

The damage caused by one water elevation-change cycle for each gate component was determined using Miner's linear damage accumulation rule (referred hereafter as Miner's rule). When using Miner's rule, higher stress ranges cause greater fatigue damage and fatigue damage is inversely related to the fatigue capacity. Miner's rule is presented in Equation 4:

$$\sum Di = \sum \frac{n_i}{N_i} \quad \text{Equation 4}$$

where D_i is the total damage, n_i is the number of cycles, and N_i is the number of cycles to failure. N_i can be calculated from the AASHTO fatigue capacity equation, here re-arranged as Equation 5:

$$N_i = A * (\Delta\sigma)^{-3} \quad \text{Equation 5}$$

where A is the detail category acquired from AASHTO Table 6.6.1.2.3-1, and $\Delta\sigma$ is the applied stress range (determined from the finite element simulations).

3.3.2. Cycle Counting

In order to evaluate fatigue damage using Equations 4 and 5, stress cycle counts and corresponding stress ranges from the analyses must be known. Two common methods of cycle counting are the rain-flow counting method and the reservoir method (see Appendix B for details on each method). Based on the graphs generated from the stress-time data (shown in Figure 22), the reservoir method was chosen and the amount of damage per section was calculated using Miner's Rule.

4. Results and Discussion from Gate Analyses

The fatigue analyses conducted for this research use the stress based method provided by AASHTO and Miner's linear damage accumulation rule. Note that the AASHTO stress based method has been used successfully to design fatigue prone bridge components (American Association of State Highway and Transportation Officials, 1988).

4.1. Fatigue Life Evaluation

Table 3 presents the accumulated fatigue damage during water-elevation change throughout the various gate components. From Table 3, and based on the applied stress range and detail category, Section F13 of Figure 22 accumulates the most fatigue damage during one water-elevation change cycle. Figure 23 shows the von Mises stress concentrations within the gate (at the stage of largest water elevation difference) along with the welded connection detail for the area with the highest fatigue damage.

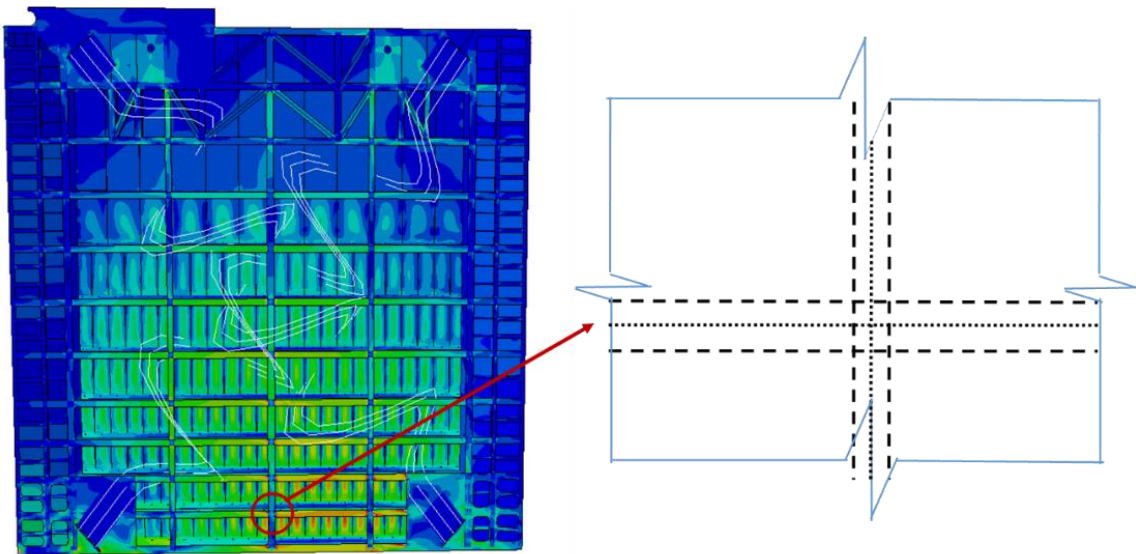


Figure 23. von Misses Stress concentrations at the point of highest loading and the connection detail for the section

Section F13 was similar in detail to sections F7-F11, F13-F14, and F20. These sections were all characterized as having the same detail category, AASHTO detail category E, but Section F13 was identified as the area of highest fatigue damage due to a high-stress concentration coupled with a small cross-sectional area when compared to the other detail

sections on the gate. Section F13 is also situated in the middle near the bottom of the gate where the hydrostatic pressure difference is the greatest. Section F13 also has a smaller cross-sectional area than section F20 (the point of highest hydrostatic pressure).

Table 3. Fatigue damage calculations of critical sections

Location	Category	Type	No.		Δf		Damage (N/Nf)	Total Damage Per Section	
			Cycles	$\Delta\sigma$	A (ksi ³)	(ksi)			
Section F7	E	7.1	1	5.945	1.10E+09	4.5	5.235E+06	1.910E-07	1.910E-07
Section F9	E	7.1	1	7.093	1.10E+09	4.5	3.082E+06	3.244E-07	3.244E-07
Section F10	E	7.1	1	22.732	1.10E+09	4.5	9.364E+04	1.068E-05	1.068E-05
Section F11	E	7.1	1	22.52	1.10E+09	4.5	9.631E+04	1.038E-05	1.038E-05
Section F12	E	7.1	1	21.584	1.10E+09	4.5	1.094E+05	9.141E-06	9.141E-06
Section F13	E	7.1	1	23.444	1.10E+09	4.5	8.537E+04	1.171E-05	1.171E-05
Section F14	E	7.1	1	23.301	1.10E+09	4.5	8.695E+04	1.150E-05	1.150E-05
Section F15	E	7.1	1	22.022	1.10E+09	4.5	1.030E+05	9.709E-06	9.709E-06
Section F16	E	7.1	1	9.807	1.10E+09	4.5	1.166E+06	8.574E-07	8.574E-07
Section F17	E	7.1	1	9.807	1.10E+09	4.5	1.166E+06	8.574E-07	8.574E-07
Section F20	E	7.1	1	22.411	1.10E+09	4.5	9.773E+04	1.023E-05	1.023E-05
Section F21	E	7.1	1	21.916	1.10E+09	4.5	1.045E+05	9.570E-06	9.570E-06
Section F22	E	7.1	1	19.854	1.10E+09	4.5	1.406E+05	7.114E-06	7.114E-06
Section Inside 1	D	1.5	1	12.534	2.20E+09	7	1.117E+06	8.950E-07	8.950E-07
Section Inside 2	D	1.5	1	10.37	2.20E+09	7	1.973E+06	5.069E-07	5.069E-07

5. Description of Detailed Fatigue Investigation for Critical Component

While the nominal stress based approach in AASHTO is useful for comparing the propensity for fracture between various details, more detailed fatigue investigations are useful for understanding the underlying fatigue causes and identifying strategies for damage prevention. For this purpose, a submodel of Section F13 is created to acquire more refined stress data from solid element types (ABAQUS element type C3D8R) within the specific section. The submodel boundary conditions are informed from the main gate model deformations such that compatibility is ensured and the submodel represents the same loading as provided for the entire gate model. Figure 24a) shows the Section F13 submodel integrated with the larger gate model while Figure 24b) shows the submodel without the gate. In addition to the refined stress data, the submodel allows simulation of weld geometry effects within the component that are impractical to include in the larger-scale gate simulations. For the submodel, section welds are modeled as triangular fillet welds, within the same submodel part, corresponding to the construction documents provided (see Figure 25).

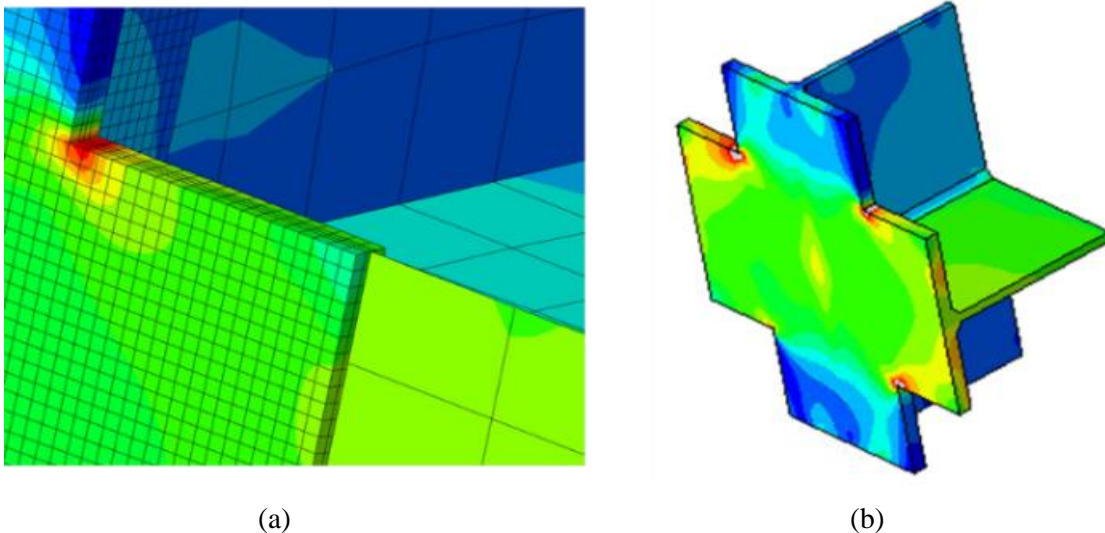


Figure 24. a) A submodel embedded in gate model with mesh view; b) 3-D of submodel with contours from loading applied to gate

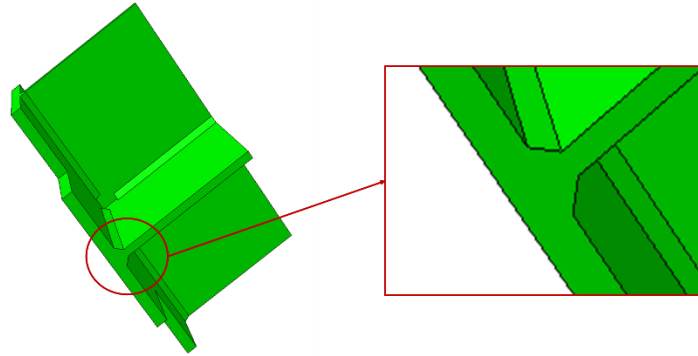


Figure 25. Triangular (fillet) Weld geometry modeled as part of the solid element model

In addition to local geometric features, the submodel considers a more refined mesh of 0.25in for capturing detailed stress information within regions having high stress gradients. Note that the main gate model had a mesh size equal to 2.5in.

A mesh convergence study helped determine the appropriate mesh size for the submodel used in this study, balancing computational expense and accuracy. In the mesh convergence study, mesh sizes at 0.25in, 0.13in, and 0.1in resulted in similar stresses (less than 0.3% difference) near the component corner (see again Figure 24(b)) indicating that the considered 0.25in mesh fully captures the stress gradient present in the component detail.

5.1. Fatigue Endurance from Constant Life Diagrams: The Goodman Criterion

Different from the nominal stress analysis using the AASHTO detail categories, local stress-states within the gate component (as informed by the submodel) can help determine fatigue damage from interacting mean stresses and stress ranges. This information is helpful in identifying strategies for fatigue mitigation within local component regions. Constant life diagrams provide the mean stress and stress range interactions for determining the fatigue endurance limit, with the Goodman criterion (see Equation 6) being commonly used for low carbon structural steels. In Equation 6, S_e is the fatigue endurance limit (having zero mean stress), S_{ult} is the material ultimate strength, and σ_a and σ_m are the stress range and mean stress as provided in Equation 6 and Equation 7 respectively.

$$\frac{\sigma_a}{S_e} + \frac{\sigma_m}{S_{ult}} \leq 1 \quad \text{Equation 6}$$

$$\sigma_m = \frac{\sigma_{max} + \sigma_{min}}{2} \quad \text{Equation 7}$$

$$\sigma_a = \sigma_{max} - \sigma_{min} \quad \text{Equation 8}$$

In Equations 7 and 8, σ_{max} is the maximum stress while σ_{min} is the minimum stress, experienced during the loading cycles. The fatigue endurance limit (S_e) was determined using the Marin equation, shown in Equation 9 (Marin, 1962).

$$S_e = k_a k_b k_c k_d k_f S'_e \quad \text{Equation 9}$$

where the modification factors $k_a, k_b, k_c, k_d,$ and k_f are respectively based on surface condition, size, load, temperature, reliability, and miscellaneous effects. S'_e is estimated using Equation 10 given by (Shigley & Mischke, 1989).

$$S'_e = \begin{cases} 0.5 * S_{ult} & S_{ult} \leq 200 \text{ ksi} \\ 100 \text{ ksi} & S_{ult} > 200 \text{ ksi} \end{cases} \quad \text{Equation 10}$$

The calculated fatigue endurance limit for the lock gate components in this study is $S_e = 18.8 \text{ ksi}$. The detailed procedure used to determine S_e and the modification factors is provided in Appendix C.

For graphical reference, Figure 26 shows the various stress components used in the Goodman criterion and Figure 27 shows an example Goodman constant life diagram bound the yield stress, referred to as a “modified” Goodman diagram. In Figure 27, the yield stress bound prevents fatigue infinite life determination under high plasticity, as different fracture mechanisms participate in the damage. Note also in Figure 27, that $\sigma_m - \sigma_a$ combinations that fall underneath the modified Goodman diagram line result in an infinite fatigue life, prior to corrosion effects.

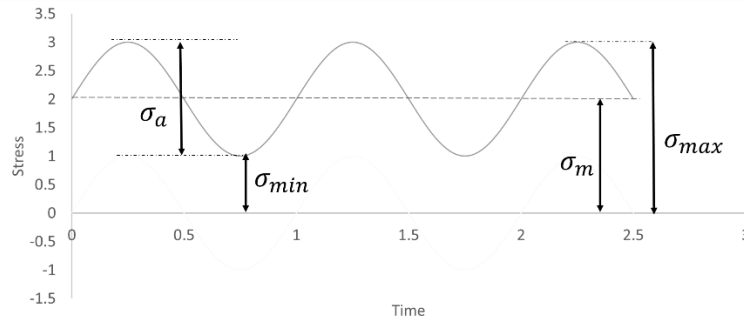


Figure 26. Components of cyclic stress

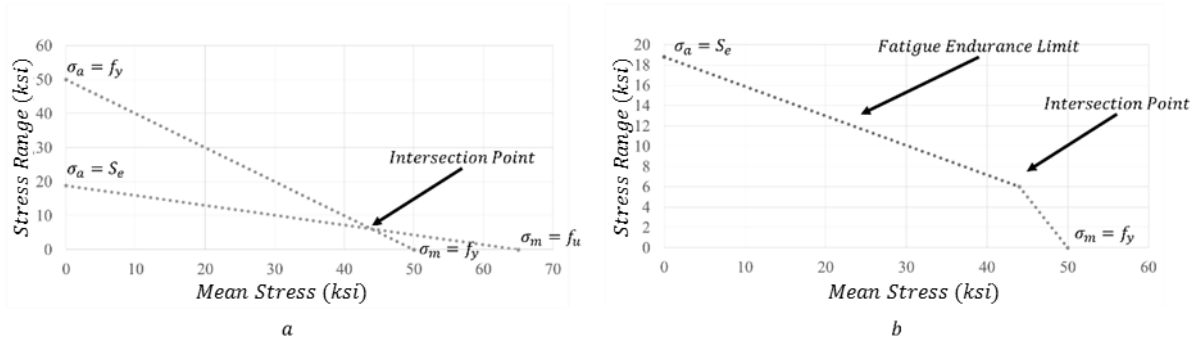


Figure 27. a) Unmodified Goodman diagram and yield line; b) Modified Goodman life diagram.

This study uses a modified Goodman diagram for determining the fatigue endurance limit of the lock gate component which is useful for determining what changes to the stress state are needed to improve the fatigue performance.

6. Required Pre-Stressing Force from Goodman Constant Life Diagram

Figure 28 shows the Goodman life diagram created using the data from the submodel and $S_e = 18.8 \text{ ksi}$. The max principal stress data from the submodel is analyzed to determine a max amplitude and mean stress using Equations 7 and 8. Section F13 has a maximum mean stress of 22.32 ksi and a maximum stress range amplitude of 21.58 ksi resulting in a finite fatigue life (as expected) as shown on the diagram (note in Figure 28 the values fall outside the Goodman line). The stress data from the submodel corresponds to one water change cycle (lockage); however, the Lockages are repeated thousands of times throughout a year, and over a period of 50 years (the design life of the gate), the amount of cycles the section experiences outside of the fatigue endurance limit can lead to cracking.

This Goodman diagram is useful in determining the required mean stress shift such that the component falls within the Goodman line and experiences infinite fatigue life, regardless of past damaging cycles. The retrofit strategy taken herein considers an external applied pre-stress such that the mean stress shift transitions the stress state to the edge of the endurance limit. The total amount of pre-stress needed for this can be found by calculating the σ_m change needed on the Goodman diagram. As a bonus, when the mean stress shifts the amplitude of the stress range also decreases as 40% of the compressive stress cycles are not considered in the fatigue evaluation (Eurocode 3: Design of Steel Structures - Part 1-9: Fatigue, 2005). Figure 28 shows the shift in the mean stress along with the reduction of amplitude which is calculated to be Equation 11.

$$\sigma_{af} = \frac{\sigma_{max} - (\sigma_{mo} - \sigma_m) - ((\sigma_{min} + 1) - (\sigma_{mo} - \sigma_m)) * 60\%}{2} \quad \text{Equation 11}$$

In Equation 11, σ_{max} is the maximum principle stress from the submodel analysis, σ_{mo} is the initial mean stress, σ_{min} is the minimum principle stress from the submodel analysis, σ_m is the new mean stress, and σ_{af} is the newly calculated amplitude stress. The change in mean

stress, $\Delta\sigma_m$, for gate Section F13 (based on the submodel analysis) is calculated to be 18.78ksi (which is rather large).

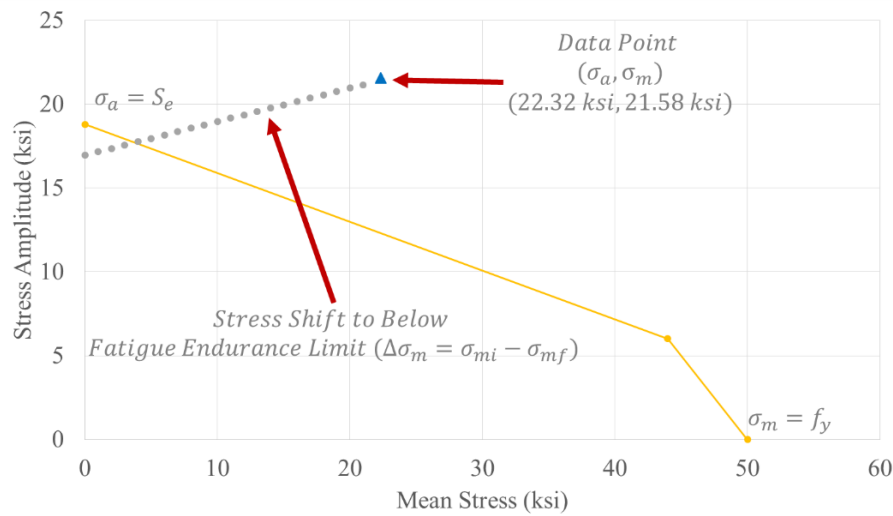


Figure 28. Modified Goodman Life Diagram with data point and stress shift

The required tension force to shift the mean stress by 18.78ksi can be found from the geometry of section and pre-stress application strategy. A free body diagram of the pre-stress retrofit configuration considered is shown in Figure 29. In Figure 29, steel plates clamp to the gate section and a pre-stressing force applied at an eccentricity (e) from the gate section. Equation 12 calculates the pre-stress force, based on the resulting section stress, pre-stress force, applied moment (from the eccentricity), and section area.

$$F_{prestress} = \frac{\Delta\sigma_m}{\left(\frac{e \cdot t_p}{z \cdot I}\right) + \left(\frac{1}{A}\right)} \quad \text{Equation 12}$$

In Equation 12, $F_{prestress}$ is the pre-stress force, $\Delta\sigma_m$ is the change in stress, e is the moment arm, t_p is the thickness of the gate component, I is the moment of inertia, and A is the area of the plate. The pre-stress force is $F_{prestress} = 8.8 \text{ kips}$. The pre-stress force is applied to the CFRP to shift the mean stress.

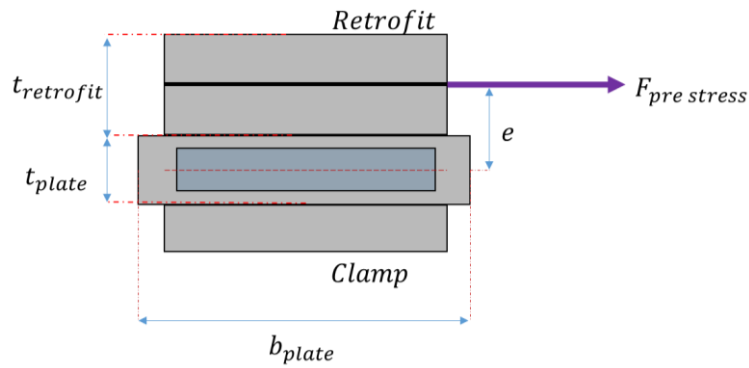


Figure 29. Free body diagram of the pre-stress force

6.1. Transfer of Pre-Stress through Friction Clamping

To transfer the required pre-stress into the gate component, a friction clamp is designed. The free body diagram shown in Figure 30 is used to assist in the calculation of the friction force, which is given by Equation 13:

$$F_{friction} = \mu * N \quad \text{Equation 13}$$

where the static coefficient of friction is μ , and N is the normal force. The total required friction force to avoid slippage of the retrofit is one half the required prestress force (see Appendices D and E for additional calculations).

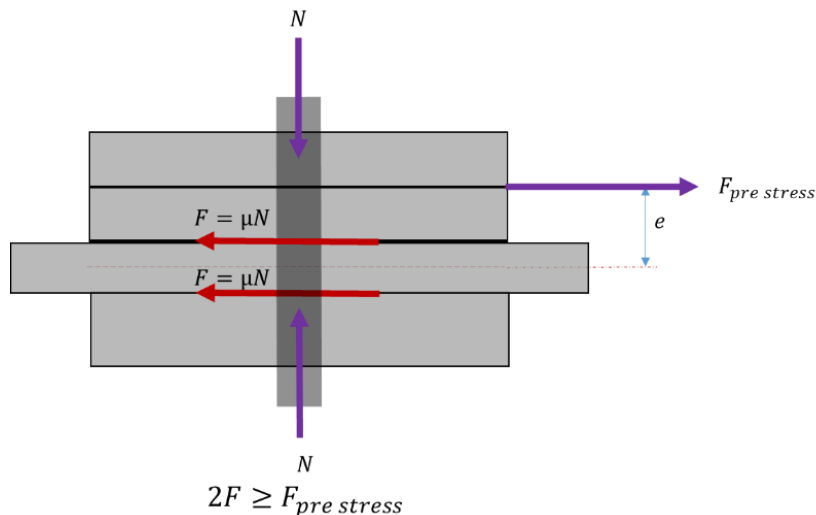


Figure 30. Free body diagram of clamp, retrofit, and section 13 to determine the required friction force from known pre-stress force

The static coefficient of friction required in Equation 13 is dependent on the interaction between surfaces. Corrosion changes the surface roughness of the steel plate, therefore the

static coefficient of friction for an un-corroded and corroded steel plate must be determined, see Figure 31. As shown in Figure 32, an experiment was conducted to determine an estimate for the static coefficient of friction between A36 steel and an uncorroded steel plate and a corroded steel plate. The static coefficient of friction for stainless steel and an uncorroded steel plate was $\mu = 0.297$ and for a corroded steel plate was $\mu = 0.343$, see Appendix D for the derivation of static coefficient of friction.



Figure 31. Corroded (bottom) and uncorroded (top) steel surfaces

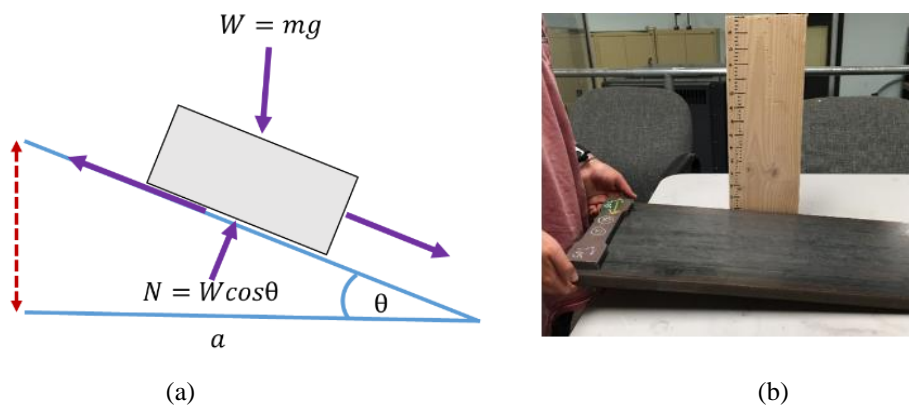


Figure 32. Static coefficient of friction test: a) static coefficient of friction free body diagram; b) test materials

7. Effect of Pre-Stress on Component Fatigue Susceptibility

To evaluate the effectiveness of the developed retrofit prestress, the designed pre-stress level of 8.8kips is applied to the critical gate component (Section F13) in the full gate finite element simulation. Figure 33 shows the application method for the pre-stress, involving nonlinear springs and rigid body connection regions (simulating plate attachments). Stiffness of the nonlinear springs considers high modulus CFRP ($E = 51,000\text{ksi}$). Also shown in Figure 33, the simulated pre-stress is applied in the horizontal and vertical directions at section F13. In the simulation, the double configuration was chosen to counteract the multi-axial stresses induced by the hydrostatic pressure difference on either side of the gate. Note that the nonlinear springs are arbitrarily attached to the gate section $16\frac{3}{8}$ in. from the component corners that experience the high stress concentration.

Resulting stress states within gate component indicate a slight reduction in mean stress (see later “Prestress Simulation Results” section); however, the shift was lower than predicted by the Goodman diagram and the component remained within the finite life region. This result indicates that higher pre-stress values are need for significant fatigue life improvement and suggests a revision is needed to the pre-stress force calculation.

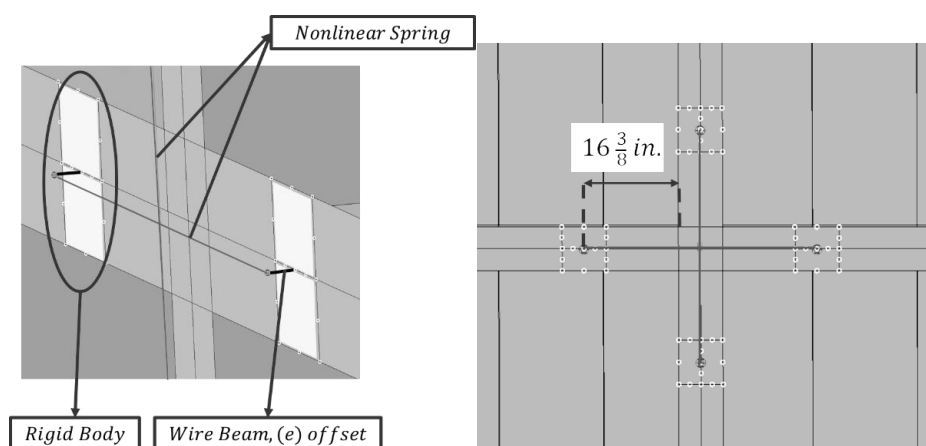


Figure 33. Retrofit application on Section F13 in the FEA model

7.1. Revised Calculations Following Retrofit Simulations

The pre-stress calculations from Section 6 were based on stress shifts within a flat steel plate; however, the geometry of the gate sections differ greatly from this assumption. A revised calculation is needed that considers the entire Section F13 cross section as seen in Figure 34 and Figure 35. From the section stresses created from the free body diagram shown in Figure 35, the new cross-section requires a larger pre-stress force of 366.6 kips (nearly 42 times greater than previously predicted). Note that this pre-stress level is required for infinite life; however, given the large force required, increases to the finite life within the critical component may be more practical.

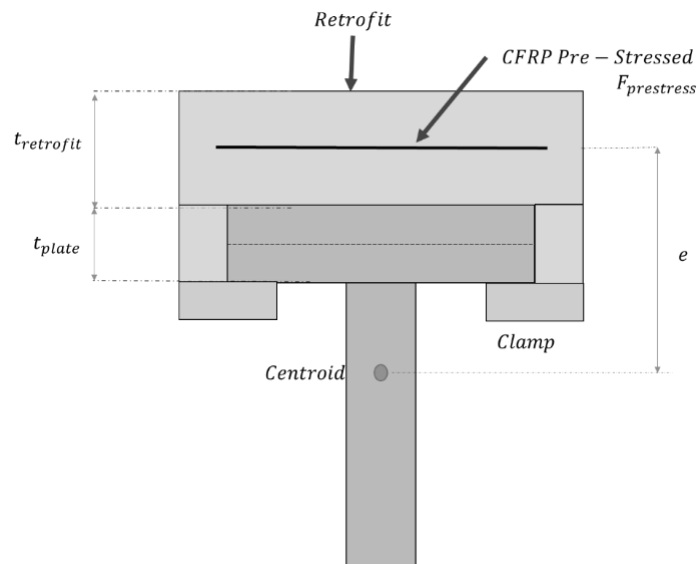


Figure 34. New Pre-stress force cross-section

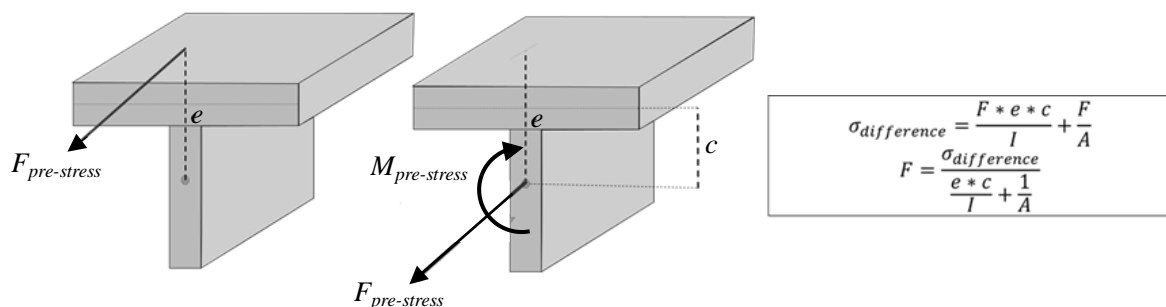


Figure 35. Free body diagram used to calculate the pre-stress force

As the required pre-stress force changes, the required friction force also changes due to the increased required pre-stress force. The greater pre-stress force creates a greater normal

force, $N = 540 \text{ kips}$, see Appendix E for calculations. The increased normal force increases the friction force to, $F_{friction} = 183.6 \text{ kips}$ (with a $\mu = 0.34$), see again Equation 13.

7.2. Pre-Stress Simulation Results

Figure 36 shows the effects of different pre-stress levels (8.8 kips, 35.2 kips, and 70.4 kips) on the stress range resulting from one lockage cycle. From Figure 36, the retrofit pre-stress level of 8.8 kips does not significantly shift the applied mean stress to have any impact on the component fatigue life. Higher pre-stress levels (arbitrarily chosen beyond 8.8kips) at 35.2 kips and 70.4 kips are capable of shifting the mean stress enough to move a portion of the stress range into compression (see Figure 36) therein prolonging the component fatigue life.

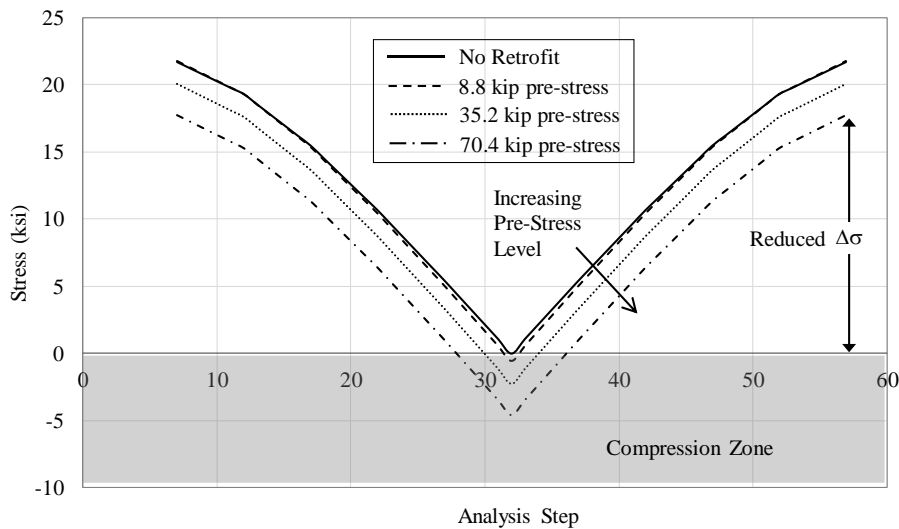


Figure 36. Stress range shift, in Section F13, due to applied CFRP pre-stress (1 lockage cycle)

Both the Goodman Life Diagram and the AASHTO life-cycle fatigue method were implemented using the data from the 3 different pre-stress force analyses. The two different methods help determine the effect of the retrofit on the stresses on gate Section F-13. Figure 37 shows a Goodman Life Diagram for Section F-13 with the mean and amplitude stresses of the section with and without the retrofit pre-stress forces. While the pre-stress forces shift the stress state in Section F13 towards the endurance limit, see Figure 37, the stress levels do not

shift below the fatigue endurance limit (which given the required pre-stress force recalculated above in section 7.1, is not surprising).

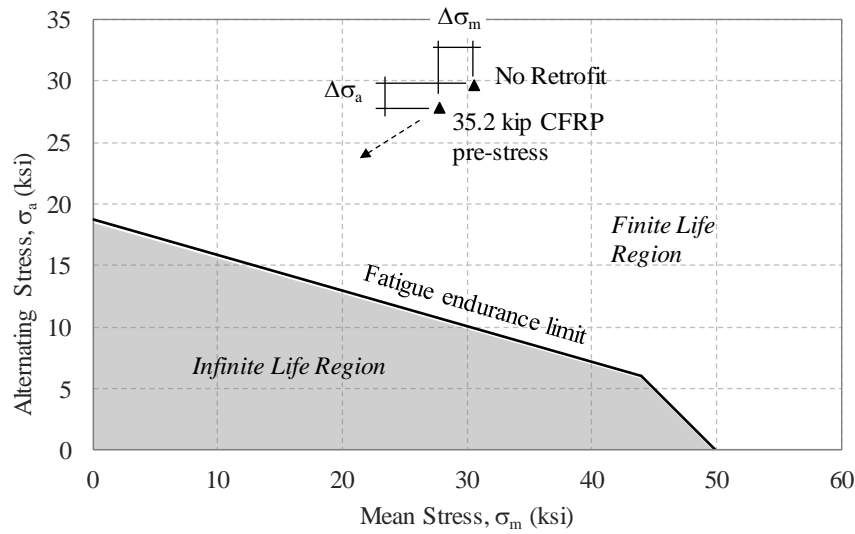


Figure 37. Goodman Life Diagram with stress shift change of Section F13 with the retrofit applying 35.2 kips pre-stress force

Table 4 shows the results of the different pre-stress forces on Section F-13. Using the average number of cycles per year for the Greenup Lock and Dam the cycles can be converted to years of operation. Table 5 shows that the pre-stress force of 35.2 kips extends the life of Section F-13 by 8.6 years (based on the average lockages for the Greenup Lock & Dam Gate 1). (Note that with a pre-stress force of 35.2 kips the required friction force is $F_{friction} = 51.8 \text{ kips}$, see Appendix E and Equation 13.)

Table 4. AASHTO Life-Cycle Fatigue from model data

Pre-Stress Force	Category	Type	# Cycles	$\Delta\sigma$ (ksi)	A (ksi ³)	Δf (ksi)	Nf (cycles)	Total Damage Per Section (SUM (N/Nf))
No Retrofit	E	7.1	1	21.696	1100000000	4.5	107711.1152	9.284E-06
8.8	E	7.1	1	21.800	1100000000	4.5	106169.019	9.419E-06
35.2	E	7.1	1	20.070	1100000000	4.5	136075.3488	7.349E-06
70.4	E	7.1	1	17.762	1100000000	4.5	196297.5537	5.094E-06

Table 5. Stresses from gate model of Greenup Lock & Dam gate 1 (35.2 kip Pre-Stress)

Average Lockages (cycles)	Total Failure Cycles (cycles)	Increase with Retrofit (cycles)	Years to Failure	Increase in life expectancy (yrs.)
3312.6	107711.1	28364.2	32.5	8.6

8. Fatigue Retrofit Prototype for Later Experimental Testing

While the prestress required for infinite fatigue life may be impractically large for a retrofit scenario, analyses indicate that moderate prestress levels are capable of significantly extending gate fatigue life (8.6 year extension at 32.5kip prestress). In the retrofit development of this study, the prestress values considered are chosen to be applied through CFRP plates; however, corrosion precautions must be taken because the CFRP material is higher on the galvanic chart than the low-carbon steel which will promote steel corrosion. To avoid adverse corrosion effects from the retrofit on the gate component, the retrofit will need to avoid contact between the CFRP and gate component (an unbonded CFRP retrofit application).

Figure 38 shows the prototype retrofit components, consisting of CFRP clamping plates for loading the CFRP and several friction clamps for transferring the CFRP prestress to the gate section. The retrofit prototype constructed in this project is made of A36 steel as a proof of concept; however, in the lock environment, a galvanic protection layer between the steel retrofit and CFRP will be added to prevent galvanic action. Appendix E presents relevant retrofit calculations related to the clamp bolt pretension levels. The CFRP pre-stress is applied by tightening bolts as seen in Figure 39. The retrofit consists of separate parts that fit within the larger friction clamp, seen in Figure 39, to facilitate attachment to the lock gate.

From Figure 39, the bolts bearing on Part (a) of the retrofit apply the pre-stress to the CFRP. The bolts allow Part (b) of Figure 39 to separate from Part (a) creating tension in the CFRP.

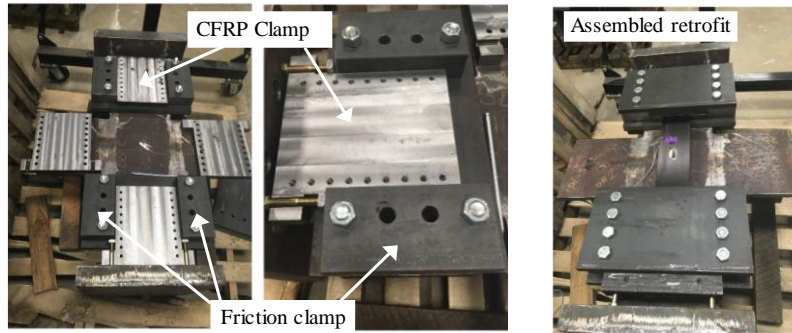


Figure 38. Retrofit components and assembled CFRP retrofit

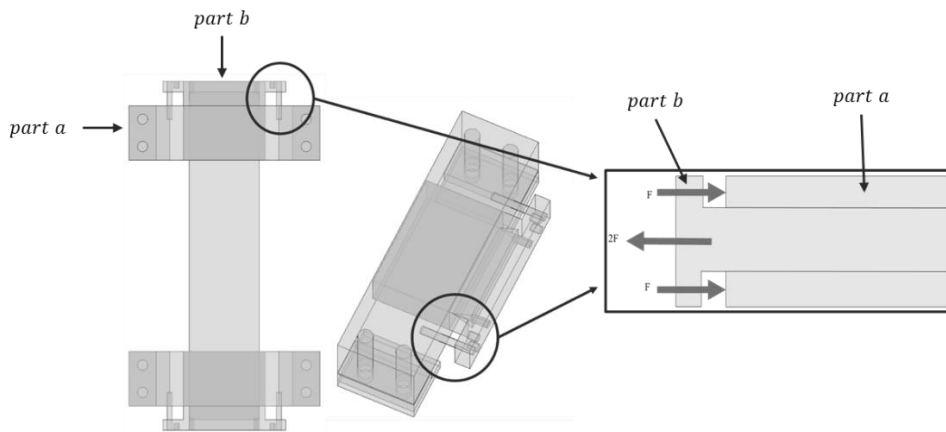


Figure 39. Cross-section of pre-stress bearing mechanism with forces applied by bolts to create the pre-stress

The retrofit uses a friction-grip clamping mechanism to keep the CFRP plate from slipping. The grated surfaces increase the coefficient of friction between the metal and CFRP material such that the pre-stress force can be transferred. As the retrofit is clamped the normal forces induced by the bolt pre-tension increases the friction force between the steel retrofit and CFRP preventing slippage. Figure 40 demonstrates the forces acting within the retrofit to keep the CFRP from slipping.

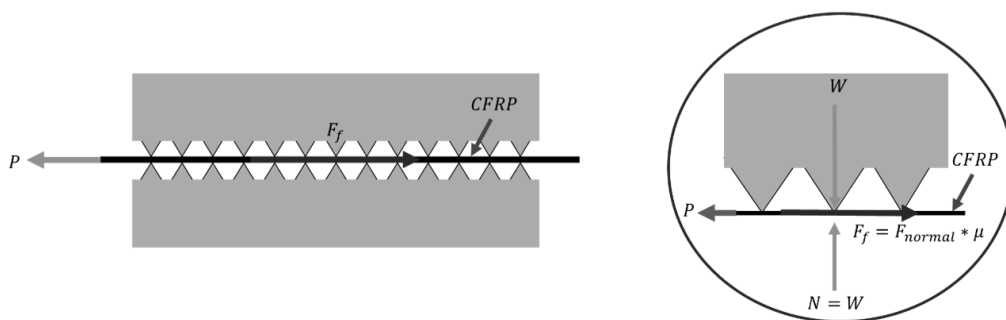


Figure 40. Cross-section view of retrofit friction grip mechanism

9. Preliminary Experimental Verification

To verify the effectiveness of the prestressing strategy and evaluate the performance of the developed retrofit, four experimental fatigue tests are proposed. This thesis will describe the four experimental tests, including the experimental setup, loading, test specimens, instrumentation, and preliminary test results from an uncracked gate specimen. Testing of the additional test specimens falls outside the scope of this work and will be presented in subsequent works by others. The following sections describe the experimental verification.

9.1. Test Matrix and Experimental Setup

A total of four full-scale component fatigue tests are proposed, representing uncracked, cracked, cracked-with-retrofit, and uncracked-with-retrofit configurations to measure the effects of the retrofit strategy. Figure 41 shows the full test matrix with the four proposed configurations, along with the experimental setup consisting of a self-reacting frame, servo-hydraulic actuator, and test specimen. The first specimen in the matrix (which will be described in this thesis) has no retrofit and is tested to determine the cycles required to initiate a crack within the gate component. The second and third specimens are on an un-cracked specimen with a retrofit, to measure retrofit effects on extending the time to crack initiation. The fourth specimen considers a fatigue crack and pre-stressed retrofit for measuring retrofit effects on crack arrest. Given the often long duration of fatigue testing, Tests 2, 3, and 4 fall outside the scope of this thesis and will be performed by others. Test 1 (on an uncracked gate specimen) will be described herein.

The self-reacting frame used to load each gate specimen (shown in Figure 41, Figure 42, and Figure 43) was stiffened for this study to reduce deflections during loading therein allowing higher frequency loadings. The frame consists of two W12×210 beam sections connected to four W12×120 column sections to create a stiff frame as seen in Figure 41 and

Figure 42. The specimen is connected to both the actuator and reaction frame (providing a load path that must travel through the specimen) with four high-strength 1-1/4” A490 bolts.

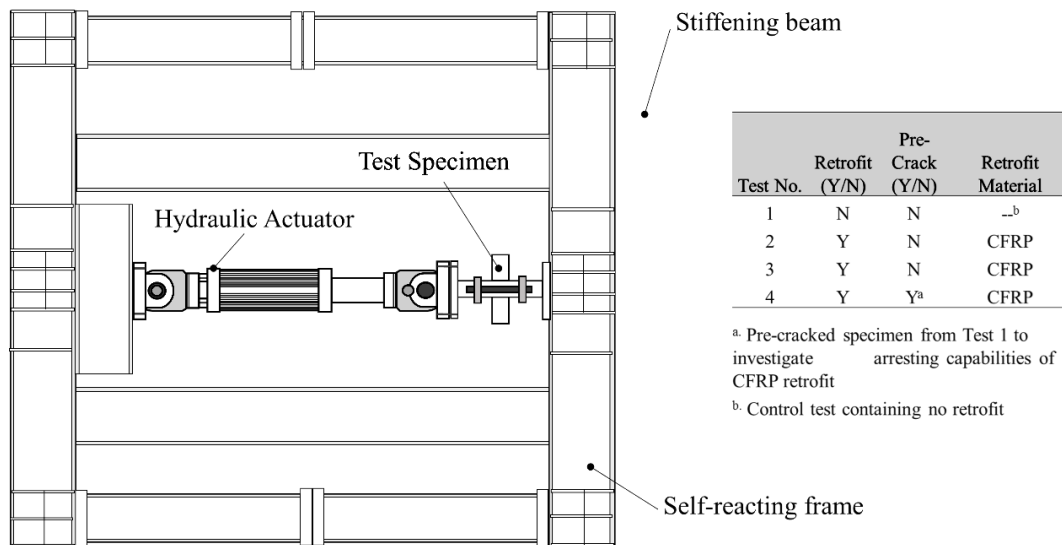


Figure 41. Diagram of top view test setup and test matrix

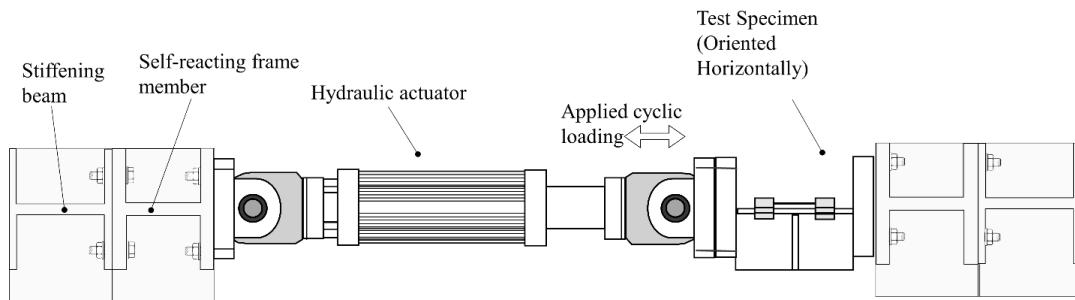


Figure 42. Diagram of test-setup side view

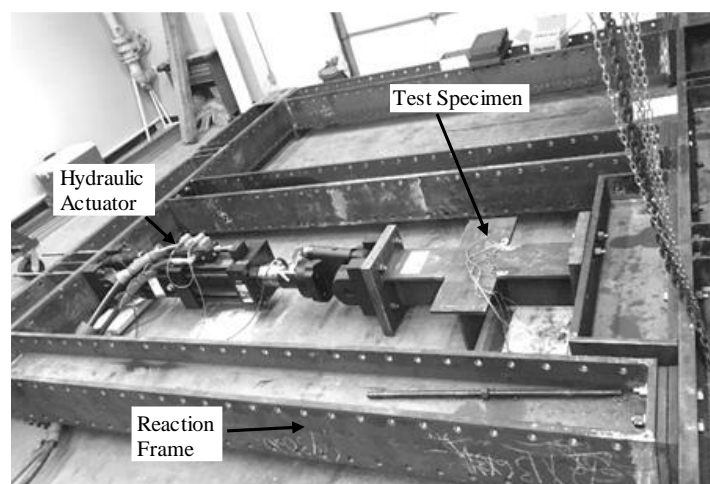


Figure 43. Test Setup

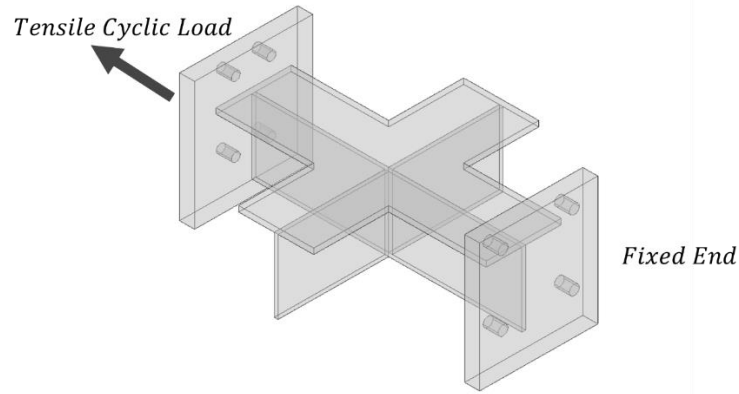


Figure 44. 3-D of the specimen with attachment plates, load, and boundary condition

9.2. Loading

Constant amplitude unidirectional tensile loading (where the specimen is loaded and unloaded during each cycle) is considered in this study, simulating normal stresses within the gate component during hydrostatic pressure changes in lock operation. To maintain a constant amplitude nominal stress within the component, all specimens are loaded in force-control. For the first specimen test, a 50 kip force is applied at a frequency of 6 Hz until fatigue cracks are detected, see Appendix F for the calculations on expected cycles to failure considering the AASHTO nominal stress approach.

9.3. Test Specimen no. 1

The full-scale specimen geometry is based on the critical fatigue detail determined from the finite element simulations. This geometry is identical to Section F13 and is fabricated from design details of the Greenup Lock and Dam provided by the United States Army Corps of Engineers. The test specimen (shown in Figure 45) is 36 inches by 30 inches by 10-3/4 inches, representing a section of gate near the critical region. Two different weld types join the test specimen plates. As shown in Figure 46, the welds consist of double-sided 3/4in bevel welds and 5/16in. fillet welds. The specimen is designed with two attachment plates connected to

each end as seen in Figure 45. These attachment plates are 2in. in thickness to avoid prying effects.

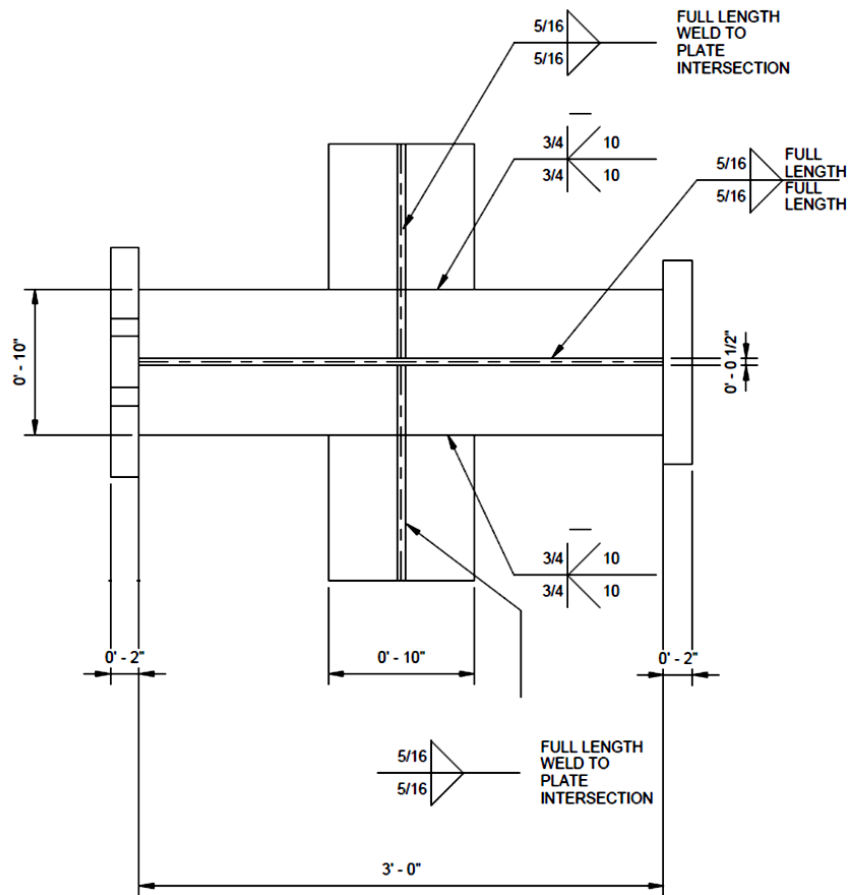


Figure 45. Section 13 specimen fabrication details

9.3.1. Model of Test Specimen

To verify that the tensile loading of the test specimen creates a similar stress state observed during gate operation, a simulation of the test specimen was performed. Boundary conditions similar to those imposed by the test setup are shown in Figure 46, and a comparison of stress contours between the full gate model and experimental setup is shown in Figure 47. From Figure 47, similar stress concentrations are observed at the test specimen corners while larger stresses are observed near the center of the plate. The stresses near the plate center are of little concern as a crack is unlikely to initiate at this location. Contours presented in Figure

47 confirm that the tensile loading imposed during by the test setup is sufficient for recreating the stress state observed at the detail corners of the actual gate.

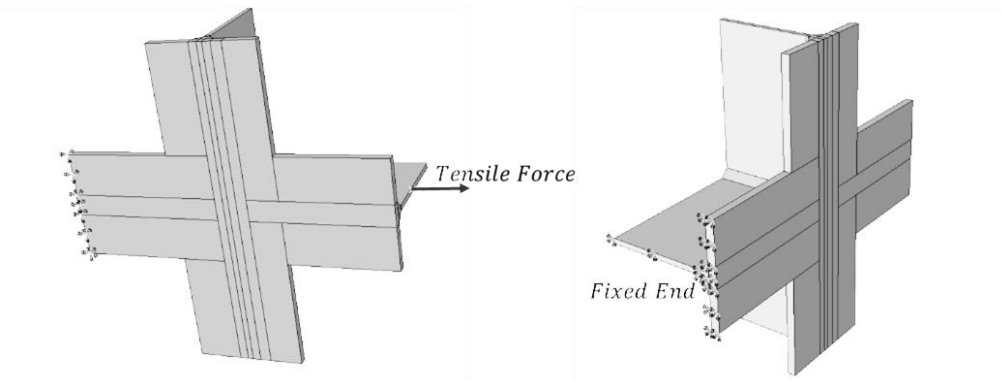


Figure 46. Boundary conditions for ABAQUS simulation of test setup

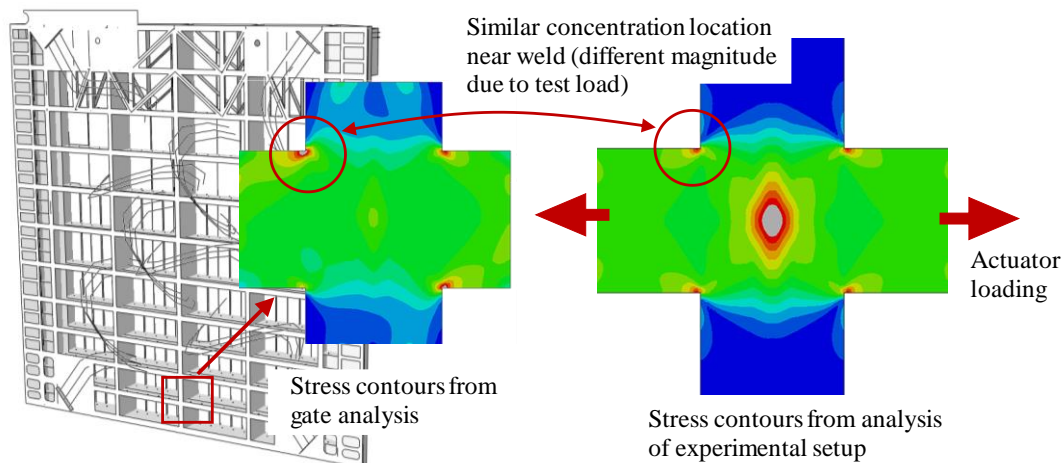


Figure 47. a) Stresses from submodel of Lock Gate; b) Stresses from model of test specimen

9.4. Instrumentation and Monitoring

The purpose of Test 1 is to measure the time required to initiate a crack within the gate specimen. In order to determine when cracking has occurred, the specimen must be monitored. The crack detection method used in this study involves visual inspection aided by dye penetrant testing and strain gage readings. While the dye penetrant allows for visual inspection of crack initiation and propagation, the strain gages help understanding of force transfer during cracking.

The gages are applied to the top and bottom of the flange plate of the specimen as shown in Figure 48. The linear gages are attached using glue and then the DAQ's wires are soldered

to gage's wires. The gages are only applied to one-half of the specimen due to the symmetry of the specimen and available DAQ connections.

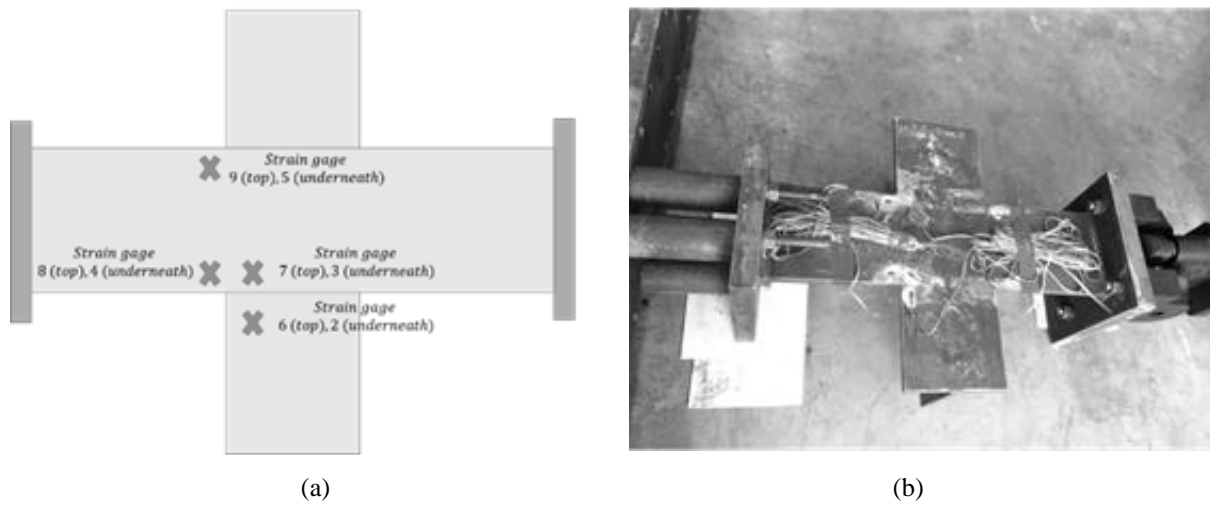


Figure 48. a) strain gage location; b) Specimen with attached strain gages

Dye penetrant is a two-part process used to detect and monitor surface cracks, see Figure 49. Before applying the penetrant, the surface should be cleaned of any dirt, grease, or oil. Then the red penetrant dye is applied on the surface and allowed to soak in for 10-30 minutes. After 10-30 minutes have passed the extra penetrant is wiped off and the white developer is sprayed on the surface. The developer draws out the penetrant from the cracks, allowing for visual inspection of the surface.

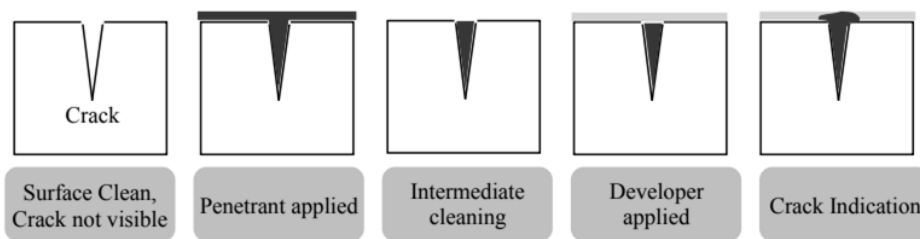


Figure 49. Dye penetrant application steps (Ovouba, 2017)

9.5. Preliminary Test Results

9.5.1. Observations

Specimen 1 achieved 8 million cycles at a force range of 50 kips before the specimen was notched (1/4in) at a weld corner to aid in crack initiation, see Figure 50. The goal of the notch was to simulate poor detailing (common in many existing gate components) and to

reduce the time required to initiate a crack for future verification of retrofit performance. Following the specimen pre-notch, 14.4 million cycles have been applied for a total of 22.4 million cycles with no observable crack detected (to date). The estimated fatigue life of the un-notched section under a 50 kip force range is 17.2 million cycles.



Figure 50. Notch at weld corner (8 million cycles)

9.5.2. Strain Gage Measurements

The strain gage data were collected every 24 hours for a period of 30 seconds. Comparisons between the pre-notch and post-notch strain results are presented in Figure 51(a) and Figure 51(b) respectively. Note that the gauge results presented are averages between gauges on the top and bottom plate sides (to cancel out any bending strains accidentally induced). As seen in Figure 51, the average strains in gauges 7 and 3 (in the direction of loading on the side of the notch) increased by more than 4.5 times after notching.

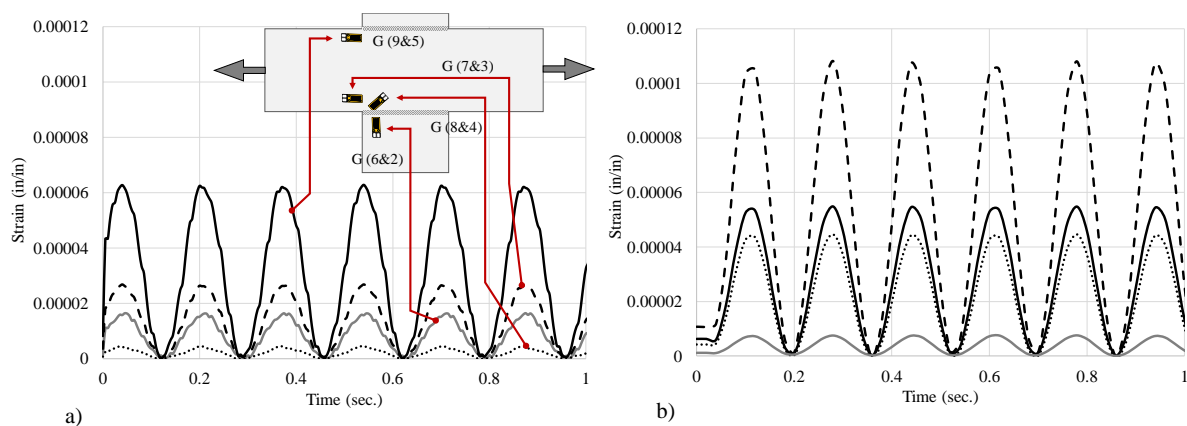


Figure 51. Recorded strains, a) pre-notch; b) post-notch

9.5.3. Dye Penetrant

Figure 52 shows the different stages of testing and dye penetrant visual inspection before and after notching of the specimen. The dye penetrant was applied at 6 million cycles (pre-notch) and at 10 million cycles (post-notch) with no visible cracks detected. The specimen will continue to be loaded by others until a crack is initiated.



Figure 52. Dye penetrant progression: a) 6 million cycles; b) 10 million cycles

10. Summary and Conclusions

This study analytically and experimentally investigated fatigue damage within common lock gate geometries, and developed fatigue mitigation strategies using tuned pre-stress levels capable of extending gate service-life. In this study, detailed finite element analyses were used to identify critical lock gate fatigue regions and evaluate pre-stress effects on locally extending component fatigue life. Fatigue and fracture mechanics theories related to constant life diagrams were used to develop retrofit strategies for preventing fatigue cracking and full-scale experimental fatigue testing of a critical lock gate component was conducted to provide a baseline for evaluation of retrofit strategies. Retrofit strategies using carbon fiber reinforced polymer (CFRP) plates having optimized pre-stress levels were created. The following conclusions result from the analytical and experimental study:

- Fatigue analysis using Miner's linear damage accumulation rule determines gate Section F13 of the Greenup Lock and Dam (see again Figure 22), as the critical fatigue region.
- Considering only the outer flange when determining the required pre-stress level for infinite fatigue using the Goodman Constant Life Diagram results in an inaccurately low estimation of required retrofit pre-stress (the required prestress force of 8.8kips was determined as too low from finite element and fatigue evaluations). The likely cause is prestress force lag into adjacent component stiffeners.
- Considering the stiffened component geometry results in a more accurate estimate of required prestress; however, the required value for the Greenup Lock and Dam is impractically large to apply in a retrofit situation (for infinite life a prestress force of 366.6kips is required).
- Pre-stress levels lower than those required for infinite life are still capable of extending gate life by several years. Simulations indicate that a pre-stress force of

35.2 kips extends the fatigue life of Section F13 in the Greenup Lock & Dam Gate by 8.6 years.

- Lock gate components fabricated using modern certified welding procedures are resilient, test Specimen 1 was subjected to 22.4 million cycles at a load range of 50kips (stress range of 4 ksi) with no observable cracks. Testing is ongoing by others continuing with the project.

11. REFERENCES

- A. Peiris, I. H. (2015). Steel Bridge Girder Strengthening Using Postinstalled Shear Connectors and UHM CFRP Laminates. *J. Perform. Constr. Facil.*
- Abaqus. (2017). *Abaqus/CAE User's Guide*, 6.14. Retrieved from Abaqus: <http://abaqus.software.polimi.it/v6.14/books/usi/default.htm>
- Alaa AL-Mosawe, R. A.-M.-L. (2015). Effect of CFRP properties on the bond characteristics between steel and CFRP laminate under quasi-static loading. *Construction and Building Materials*, 98, 489-501.
- Alkhrdaji, T. (2015, June). Strengthening of Concrete Structures using FRP Composites. *Structure Magazine*, pp. 18-20. Retrieved from Structure Magazine.
- American Association of State Highway and Transportation Officials. (1988). *AASHTO LRFD Bridge Design Specifications* (2nd ed.). AASHTO.
- American Association of State Highway and Transportation Officials. (2012). *AASHTO LRFD Bridge Design Specifications* (6th ed.). AASHTO.
- Anderson, T. (2005). *Fracture Mechanics Fundamentals and Applications* (Third ed.). Boca Raton: CRC Press.
- B. Kaan, F. A.-G. (2012). Fatigue Enhancement of Welded Details in Steel Bridges using CFRP Overlay Elements. *ASCE Journal of Composites for Construction*, 16(2).
- Barbara A. Kelly, R. J. (1997). Restored Fatigue Life with Repair Welds. *International Society of Offshore and Polar Engineers*.
- D. Schnerch, A. R. (2008). Flexural Strengthening of Steel Bridges with High Modulus CFRP Strips. *Journal of Bridge Engineering*, 13(2), pp. 192-201.
- E. Ghafoori, M. M. (2011). Analytical calculation of stress intensity factor of cracked steel I-beams with experimental analysis and 3D digital image correlation measurements. *Engineering Fracture Mechanics*, 3226-3242.
- E. Ghafoori, M. M. (2015, January). Design criterion for fatigue strengthening of riveted beams in a 120-year-old railway metallic bridge using pre-stressed CFRP plates. *Composites*, 68, pp. 1-13. Retrieved 2016
- E. Ghafoori, M. M. (2016). Fatigue strengthening of riveted girders in a historic railway metallic bridge in Switzerland using pre-stressed un-bonded CFRP laminates. *International Conference on Bridge Maintenance, Safety and Management*.
- E.N. Gregory, G. S. (n.d.). *Welded repair of cracks in steel bridge members*. National Cooperative Highway Research Program. Washington D.C.: Transportation Research Board.
- Eurocode 3: Design of Steel Structures - Part 1-9: Fatigue*. (2005). Brussels, Belgium: European Committee for Standardization .

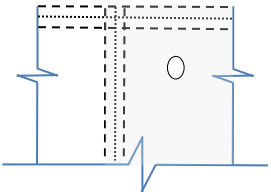
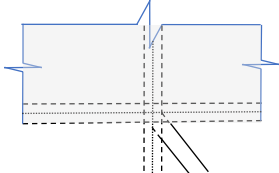
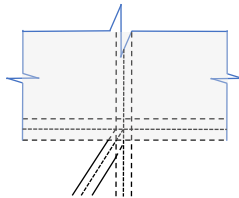
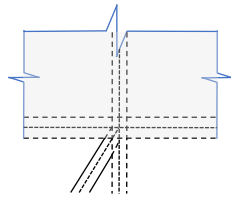
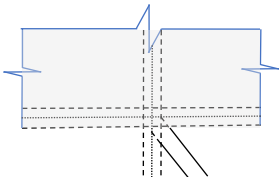
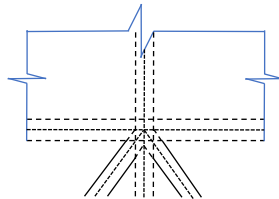
- Fabio Matta, C. A. (2007). Unbonded CFRP Bar System for External Post-Tensioning. *Composites and Polycon*.
- Gangloff, R. (2005). Environmental Cracking. In R. Gangloff, *Corrosion Tests and Standards* (2nd ed.).
- Glass, P. (2012, July 25). *Head Lock*. Retrieved from Workboat: <https://www.workboat.com/archive/head-lock/>
- Grimwood, H. (2016, September 8). *Corps of Engineers ready to open lock and dam*. Retrieved from NewsOK: <http://newsok.com/article/feed/1071404>
- Hussam Mahmoud, A. C. (2017). Fatigue and Fracture life-cycle Cost Assessment of A Miter Gate with Multiple Cracks. *Engineering Failure Analysis*.
- James, M. (2016, April 7). *Lock repair to start at Greenup: Slower traffic for five months, recreational locking restricted*. Retrieved from The Daily Independent: http://www.dailyindependent.com/news/lock-repair-to-start-at-greenup/article_2017f136-fcf8-11e5-af38-2349aba4c350.html
- Kentaro Yamada, Y. S. (1986). Weld Repair of Cracked Beams and Residual Fatigue Life. *JSCCE Structural Engineering/Earthquake Engineering*, 3(2), 373-382.
- Kopeliovich, D. (2012). *Carbon Fiber Reinforced Polymer Composites*. Retrieved from SubstTech Substances & Technologies: http://www.substech.com/dokuwiki/doku.php?id=carbon_fiber_reinforced_polymer
- M. Tavakkolizadeh, H. S. (2003, February 1). Fatigue Strength of Steel Girders Strengthened with Carbon Fiber Reinforced Polymer Patch. *Journal of Structural Engineering*, 129(2), pp. 186-196. doi:10.1061/(ASCE)0733-9445(2003)129:2(186)
- MARAD. (2017). *Ships and Shipping*. Retrieved from MARAD-Maritime Administration: <https://www.marad.dot.gov/ships-and-shipping/dot-maritime-administration-americas-marine-highway-program/>
- Marin, J. (1962). *Mechanical Behavior of Engineering Materials*. Englewood Cliffs, NJ: Prentice-Hall.
- Merriam Webster. (2017). *Merriam Webster*. Retrieved from Lockage: <https://www.merriam-webster.com/dictionary/lockage>
- Mertz, D. (2012). Design for Fatigue. In D. Mertz, *Steel Bridge Design Handbook* (Vol. 12).
- NACE International. (2017). *Corrosion Fatigue*. Retrieved from NACE International: <https://www.nace.org/Corrosion-Central/Corrosion-101/Corrosion-Fatigue/>
- Ovouba, B. (2017). *On the Fatigue of Headed Shear Studs in Steel-Concrete Composite Bridge Girders*. Fayetteville: University of Arkansas. Retrieved October 6, 2017
- Prem Pal Bansal, R. S. (2016). Retrofitting of RC girders using pre-stressed CFRP sheets. *Steel and Composite Structures*, 20(4), 833-849. Retrieved 2017

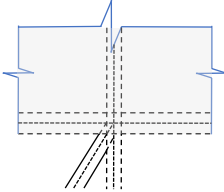
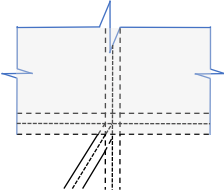
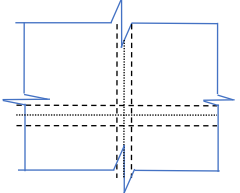
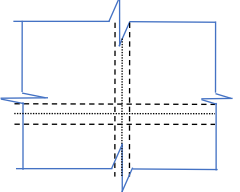
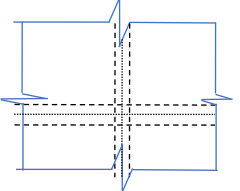
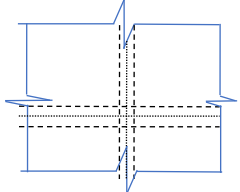
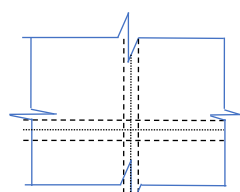
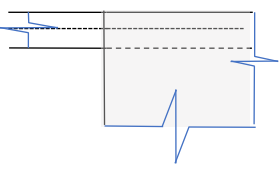
- Riveros, G. (2009). *Numerical Investigation of Miter Gates*. U.S. Army Corp of Engineers.
- Robert J. Dexter, J. M. (2013). *Manual for Repair and Retrofit of Fatigue Cracks in Steel Bridges*. Minneapolis: U.S. Department of Transportation Federal Highway Administration.
- Shigley, J. E., & Mischke, C. R. (1989). *Mechanical Engineering Design* (5th ed.). New York: McGraw-Hill.
- Stefano Caramelli, P. C. (1997). Repair techniques for the rehabilitation of. *Proceedings IABSE Workshop: Evaluation of Existing Steel and Composite Bridges*, (pp. 161-169). Lausanne.
- Sungnam Hong, S.-K. P. (2015). Concrete beams strengthened with prestressed unbonded carbon-fiber-reinforced polymer plates: An experimental study. *Polymer Composites*. doi:10.1002/pc.23833
- T.C. Miller, M. C. (2001). Strengthening of a Steel Bridge Girder using CFRP Plates. *Journal of Bridge Engineering*, 6(6), pp. 514-522.
- The Port of Pittsburgh Commission. (2017). *The Port District and the Inland Waterway System*. Retrieved from Port of Pittsburgh Commission: <http://www.port.pittsburgh.pa.us/index.aspx?page=127>
- U.S. Army Corps of Engineers. (1999). *Inland Waterway Navigation: Value to the Nation*. U.S. Army Corps of Engineers. Retrieved from <http://www.sas.usace.army.mil/Portals/61/docs/lakes/thurmond/navigate.pdf>
- U.S. Army Corps of Engineers. (2017). *Braddock Locks and Dams*. Retrieved from U.S. Army Corps of Engineers-Pittsburg District: <http://www.lrp.usace.army.mil/Missions/Navigation/Locks-and-Dams/Braddock-Locks-Dam/>
- U.S. Army Corps of Engineers. (2017). *Emsworth Locks and Dams*. Retrieved from U.S. Army Corps of Engineers: <http://www.lrp.usace.army.mil/Missions/Navigation/Locks-and-Dams/Emsworth-Locks-Dams/>
- U.S. Army Corps of Engineers. (2017). *Hildebrand Lock Dam*. Retrieved from U.S. Army Corps of Engineers-Pittsburg District: <http://www.lrp.usace.army.mil/Missions/Navigation/Locks-and-Dams/Hildebrand-Lock-Dam/>
- U.S. Army Corps of Engineers. (2017). *Infrastructure Report Card: Inland Waterways*. ASCE.
- U.S. Army Corps of Engineers Mississippi Valley Division. (2016). *Illinois Waterway Locks and Dams: Rock Island District*. Chicago: U.S. Army Corps of Engineers.
- United States Army Corps of Engineers. (2015, February 27). *Lock and Dam Winter Maintenance*. St. Paul District Projects. Retrieved from <http://www.mvp.usace.army.mil/Home/Projects/Article/571183/lock-and-dam-winter-maintenance/>

- Y. Huawen, C. K. (2010). Fatigue Performance of Tension Steel Plates Strengthened with Prestressed CFRP Laminates. *ASCE Journal of Composites for Construction*, 14(5), pp. 609-615.
- Y. Huawen, C. K. (2010). Fatigue Performance of Tension Steel Plates Strengthened with Prestressed CFRP Laminates. *Journal of Composites for Construction*.
- Yail J. Kim, K. A. (2011, February 21). Fatigue Behavior of Damaged Steel Beams Repaired with CFRP Strips. *Engineering Structures*, 33, pp. 1491-1502. doi:10.1016/j.engstruct.2011.01.019

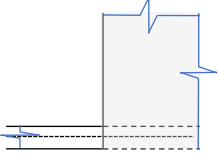
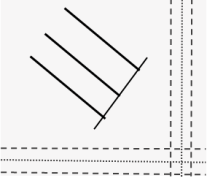
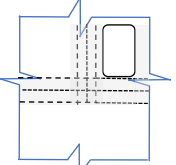
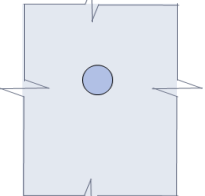
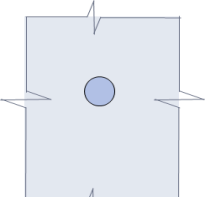
Appendix A. Identification of Critical Sections

Table 6: List of identified critical sections, detail diagram, AASHTO category, and damage

Section	Sketch	Type	Category	Damage (N/N _t)
Section F1		1.5	D	No Damage
Section F2		7.1	E	No Damage
Section F3		7.1	E	No Damage
Section F3		7.1	E	No Damage
Section F4		7.1	E	No Damage
Section F5		6.1	E	No Damage

Section F6		7.1	E	No Damage
Section F6		7.1	E	No Damage
Section F7		6.1	E	1.91032E-07
Section F8		6.1	E	No Damage
Section F9		6.1	E	3.24412E-07
Section F10		6.1	E	1.06787E-05
Section F11		6.1	E	1.03828E-05
Section F12		7.1	E	9.1412E-06

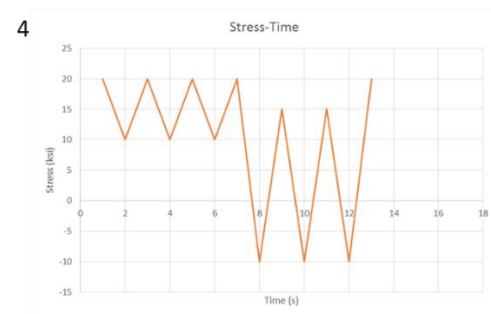
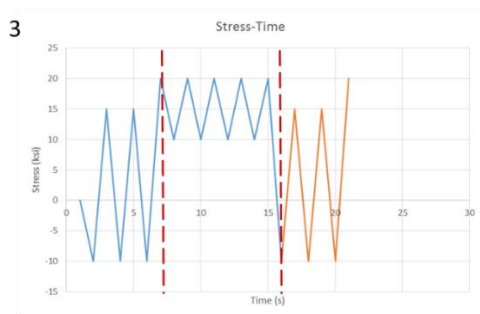
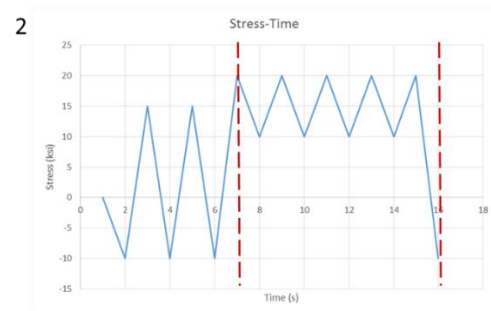
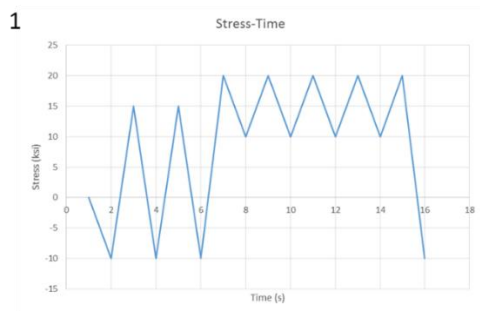
Section F13		6.1	E	1.17139E-05
Section F14		6.1	E	1.15013E-05
Section F15		7.1	E	9.70907E-06
Section F16		7.1	E	8.57359E-07
Section F17		7.1	E	8.57359E-07
Section F18		5.3	C	No Damage
Section F19		7.1	E	No Damage
Section F20		6.1	E	1.02327E-05
Section F21		6.1	E	9.56954E-06

Section F22		7.1	E	7.11418E-06
Section F23		5.3	C	No Damage
Section F24		7.1	E	1.37003E-06
Section Inside Hole 1		1.5	D	8.95048E-07
Section Inside Hole 2		1.5	D	5.0689E-07

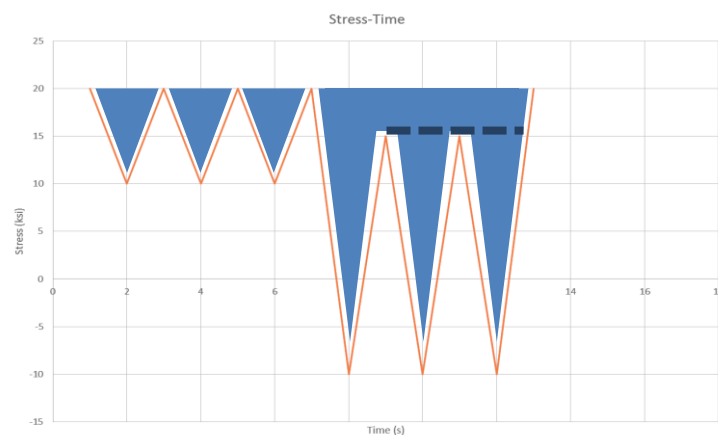
Appendix B. Reservoir Cycle Counting Procedure

Cycle counting is used to get data from stress-time graph for fatigue analysis. There are two methods for cycle counting: reservoir cycle counting and rain flow cycle counting. The reservoir counting method was chosen because it was a better fit for the stress-time graphs from the output data.

1. Shift part of the cycles so that the highest peaks are the starting point and ending point.

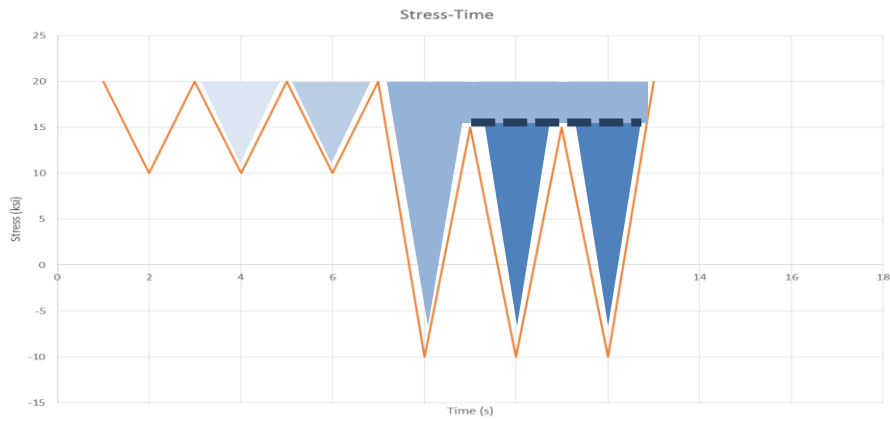


2. Imagine that the new graph is a reservoir filled with water.



3. Drain the reservoirs from the bottom of each valley.

- a. Note the stress range from each drainage
- b. Note the number of cycles per drainage. (Each valley is a cycle)



4. Create a table with the number of cycles at each stress range.

No. Cycles	Stress Range [ksi]
3	10
1	30
2	20

Appendix C. Goodman S_e Calculations

This section describes how to calculate the fatigue endurance limit (S_e) using the Marin Equation. The 5th edition of *Mechanical Engineering Design* describes the process used to acquire the fatigue endurance limit (Shigley & Mischke, 1989). The Marin equation is shown here as Equation 14.

$$S_e = k_a k_b k_c k_d k_f S'_e \quad \text{Equation 14}$$

The endurance limit, S'_e , is based on results from a rotating beam specimen, and is calculated using Equation 15.

$$S'_e = \begin{cases} 0.5 * S_{ult} & S_{ult} \leq 200 \text{ ksi} \\ 100 \text{ ksi} & S_{ult} > 200 \text{ ksi} \end{cases} \quad \text{Equation 15}$$

Modification Factors

Surface factor k_a

Cracks often initiate at the surface of the material. The surface modification factor assesses the quality of the finished surface along with the tensile strength of the material. Equation 16 calculates the factor k_a .

$$k_a = a S_{ult}^b \quad \text{Equation 16}$$

Table 7 determines the coefficients a and b . The component is hot-rolled with corresponding values for the coefficients determined from Table 7, and an ultimate strength of $S_{ut} = 65 \text{ ksi}$ for A572 steel. The surface factor is $k_a = 0.7189$.

Table 7: Parameters for Marin surface modification factor

Surface Finish	Factor a, S_{ut} given in ksi	Exponent b
New Ground	1.43	-0.085
Machined or cold-drawn	2.7	-0.265
Hot-rolled	14.4	-0.718
As-forged	39.9	-0.995

Size factor k_b

The size factor is based on volume. The size factor for the rotating bar specimen is determined by fitting a curve to experimental results. Volume affects the probability of failure as the probability of stress interaction with a critical flaw increases as the volume increases decreasing the endurance limit (Marin, 1962). Equation 17 calculates k_b for members that are subjected to bending and torsion.

$$k_b = \begin{cases} 0.879d^{-0.107} & 0.11 \leq d \leq 2 \text{ in} \\ 0.91d^{-0.157} & 2 < d \leq 10 \text{ in} \end{cases} \quad \text{Equation 17}$$

There is no size effect for axial loading, therefore $k_b = 1$. An effective diameter, d_e is used in place of d , in Equation 4, when the member is non-circular. The effective diameter d_e is calculated in Equation 18.

$$d_e = 0.808\sqrt{bh} \quad \text{Equation 18}$$

The variable b is the base and h is the height of the member's cross-section. Equations for other cross-sections are given in *Mechanical Engineering Design, 5th Ed* (Shigley & Mischke, 1989).

The component is under bending and has a rectangular cross-section. The variables $b = 10 \text{ in}$ and $h = \frac{3}{4} \text{ in}$, therefore the effective diameter is $d_e = 2.21 \text{ in}^2$. The size factor is $k_b = 0.803$.

Load factor k_c

The way a component is loaded affects its fatigue strength. The load factor k_c considers axial, bending, or torsional loading, see Equation 19. Estimated values for k_c are given below. The component experiences bending therefore $k_c = 1.0$.

$$k_c = \begin{cases} 1.0 & \text{Bending} \\ 0.85 & \text{Axial} \\ 0.59 & \text{Torsion} \end{cases} \quad \text{Equation 19}$$

Temperature factor k_d

Surface temperature affects the endurance limit of the component because the ultimate strength, S_{ut} , varies with temperature. Higher temperatures cause the yield strength to decrease leading to ductile failure. Lower temperatures can cause a brittle failure. Equation 20 calculates the temperature factor.

$$k_d = 0.975 + 0.432(10^{-3})T_f - 0.115(10^{-5})T_f^2 + 0.104(10^{-8})T_f^3 - 0.595(10^{-12})T_f^4 \quad \text{Equation 20}$$

The temperature variable, T_f , is in Fahrenheit and within the range $70 \leq T_f \leq 1000$ °F. The temperature factor, at the average water temperature $T_f = 75$ °F, is $k_d = 1.001$.

Reliability factor k_e

As the percent of reliability increases the reliability factor k_e decreases. Fatigue is based on the number of cycles a component is subjected to and the S-N curves used to determine fatigue endurance limits are based on statistical data. Figure 59 shows the uncertainty of the S-N curve data leads to a mean strength value within a standard deviation in a normal distribution plot. Reliability is the degree that a measurement, data, or calculation can be trusted. As reliability increases the component failure area, illustrated in Figure 59, decreases and along with the reliability factor. Table 8 gives percentages of reliability with the corresponding reliability factor, k_e . A conservative estimate of 50% reliability was chosen for section 13, and the reliability factor is, $k_e = 1.0$.

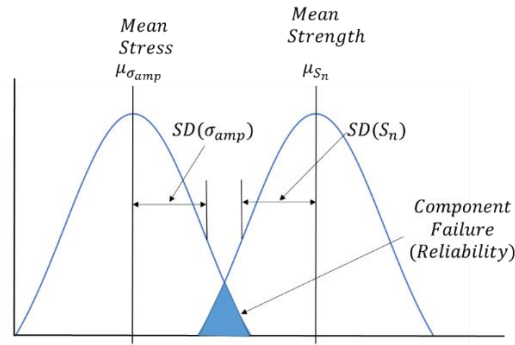


Figure 59: Mean stress and strength curves

Table 8: Reliability factors corresponding to 8% standard deviation of the endurance limit

Reliability, %	Reliability Factor, k_e
50	1.000
90	0.897
95	0.868
99	0.814
99.9	0.753
99.99	0.702
99.999	0.659
99.9999	0.620

Miscellaneous-Effects factor k_f

The miscellaneous-effects factor takes into consideration other environmental factors that can affect the fatigue endurance limit. Miscellaneous-effects factor considers influences such as corrosion, electrolytic plating, metal spraying, cyclic frequency, and frottage corrosion (Shigley & Mischke, 1989). Since these values are environmentally dependent and hard to determine the miscellaneous-effects factor is assumed to be $k_f = 1.0$.

Calculating S_e

The endurance limit, S_e , is calculated for section 13. Assumptions were made about the type of steel, temperature, reliability percentage, and other environmental factors to determine the different factors. The cross-sectional area of section 13 was calculated to determine the size

factor. Section 13 is in bending and therefore the load factor coefficient chosen corresponds with bending. Table 9 summarizes the different factors.

Table 9: Calculated Marin modification factors summary and modified endurance limit

Factor	Value
k_a	0.719
k_b	0.803
k_c	1.000
k_d	0.999
k_e	1.000
k_f	1.000
S'_e	32.500 ksi

The calculated endurance limit, using Equation 21, is $S_e = 18.8 \text{ ksi}$.

$$S_e = k_a k_b k_c k_d k_f S'_e \quad \text{Equation 21}$$

Appendix D. Friction Test Derivation

The coefficient of static friction between rusted steel and stainless steel is determined through an experiment. The rusted steel is used as a ramp that the stainless-steel block slides down. The test consists of raising the ramp until the stainless piece begins to move. Once the stainless-steel block begins to move the gravity force on the block overcomes the friction force, see Figure 60 b. Figure 60 demonstrates how the ramp experiment allows for the static friction of coefficient to be calculated. Figure 33 in Section 8.1 shows the two steel blocks used for the test (non-corroded and corroded) and the stainless-steel ramp.

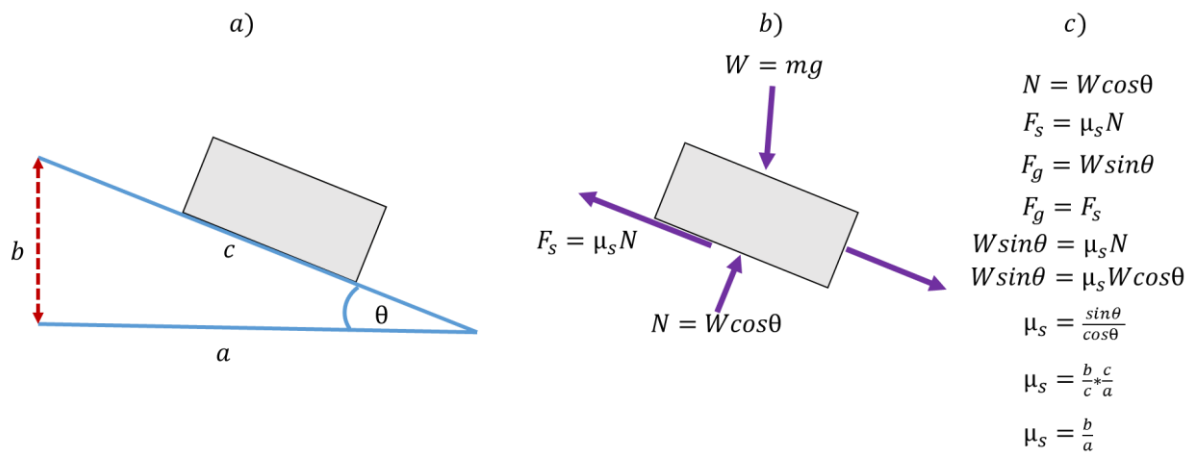


Figure 60: Static friction of coefficient test and derivation

Appendix E. Friction Clamp Calculations

The friction force is calculated using a free body diagram (Figure 61), a known static coefficient of friction (μ), and a known pre-stress force (F_{pre}). There are two planes of friction, as seen in Figure 56. The two planes of friction divide the required clamping force (N) in half. The static coefficient of friction derived in Appendix D is $\mu = 0.34$. The previously derived pre-stress, Section 8, force is $F_{pre} = 366.57 \text{ kips}$. The calculated downward force is $N = 540 \text{ kips}$, see Figure 61.

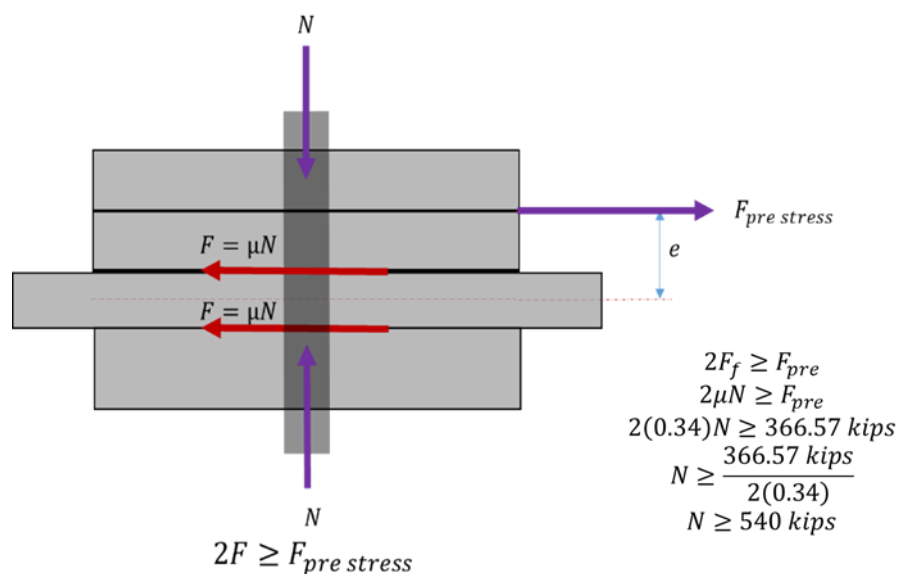


Figure 61: Free body diagram of friction clamp and derivation

Appendix F. Cycle Estimation for Experimental Test

The estimated number of cycles to reach damage is determined using AASHTO chapter 6. Table 6.6.1.2.3-1 from AASHTO chapter 6 gives the category, constant (A) (ksi^3), and threshold (ΔF_{TH}) (ksi). The stress range (ΔF_N) is determined from the gate model max-in-plane stress data. Equation 22, from AASHTO chapter 6 equation 6.6.1.2.5-2, is used to calculate the number of cycles to damage at the given stress range.

$$N = \frac{A}{\Delta F_N^3} \quad \text{Equation 22}$$

At the stress range $\Delta F = 24.467 \text{ ksi}$, calculated from the gate model, the number of cycles is $N = 73,468$. Due to the capability of the hydraulic actuator the tensile force applied during testing is 50 kips. The area the load is applied to is $A_{area} = 12.5 \text{ in}^2$. At the tensile load of $P = 50 \text{ kips}$ and $A_{area} = 12.5 \text{ in}^2$ the stress $\Delta F = 4 \text{ ksi}$. The number of cycles to damage at $\Delta F = 4 \text{ ksi}$ is $N = 17.2 * 10^6$.